The PVEMC Experiment

First Measurement of the Flavor Dependence of Nuclear PDF Modification Using Parity-Violating Deep Inelastic Scattering

A Proposal to PAC 49

Spokespersons: John Arrington, Rakitha Beminiwattha, Dave Gaskell, Juliette Mammei, Paul E. Reimer

May 24, 2021

J. Arrington[*,†], S. Li, E. Sichtermann, Y. Mei
Lawrence Berkeley National Laboratory

R. Beminiwattha[*], S. P. Wells, N. Simicevic
Louisiana Tech University

D. Gaskell[*], J. Benesch, A. Camsonne, J. P. Chen, S. Covrig, J.-O. Hansen, C. E. Keppel, and M.-M. Dalton, R. Michaels
Thomas Jefferson National Accelerator Facility

J. Mammei[*], W. Deconinck, M. Gericke, P. Blunden
University of Manitoba

P. E. Reimer[*], W. R. Armstrong, I. C. Cloët
Argonne National Laboratory

S. Barkanova
Acadia University

K. Aniol
California State University, Los Angeles

D. S. Armstrong
College of William and Mary

H. Gao, X. Li, T. Liu, C. Peng, W. Xiong, X. Yan, and Z. Zhao
Duke University

P. Markowitz and M. Sargsian
Florida International University

A. Aleksejevs
Grenfell Campus of Memorial University

D. McNulty
Idaho State University

V. Bellini, C. Sutera
INFN - Sezione di Catania

J. Beričič, S. Širca, and S. Štajner
Jožef Stefan Institute and University of Ljubljana, Slovenia

J. Dunne, D. Dutta and L. El Fassi
Mississippi State University

P. M. King and J. Roche
Ohio University, Athens, Ohio

M. Hattawy
Old Dominion University, Norfolk, Virginia

R. Gilman, K. E. Mesick
Rutgers University

A. Deshpande, C. Gal, N. Hirlinger Saylor, T. Kutz, and Y.X. Zhao
Stony Brook University

R. Holmes and P. Souder
Syracuse University

A. W. Thomas
University of Adelaide, Australia

Y. Kolomensky

University of California, Berkeley

A. J. Puckett
University of Connecticut

K. S. Kumar, R. Miskimen
University of Massachusetts, Amherst

N. Fomin
University of Tennessee, Knoxville

X. Bai, D. Di, K Gnanvo, C. Gu, N. Liyanage, H. Nguyen, K. D. Paschke, V. Sulkosky, and X. Zheng
University of Virginia

N. Kalantarians
Virginia Union University

and the SoLID Collaboration

*Spokesperson
†Contact, JArrington@lbl.gov

Contents

1 Executive Summary

We propose a clean and precise measurement of the flavor dependence of the EMC effect using parity-violating deep inelastic scattering on a ^{48}Ca target. This measurement will provide evidence of nuclear parton distribution function modification that is dependent on the neutron excess of a nucleus. Such an effect would represent new and important information about our understanding of nucleon modification at the quark level. While this effect has been known for over 30 years, it is still not fully understood theoretically and there is essentially no experimental constraint on the flavor dependence. In addition, a flavor-dependent nuclear pdf modification could have significant impact on a range of processes, including neutrino-nucleus scattering, Nuclear Drell-Yan processes, or e-A observables at a future EIC.

Parity-violating deep inelastic scattering generates an asymmetry between helicity states of longitudinally polarized electrons scattered from a ^{48}Ca unpolarized target. This asymmetry arises from the interference between the virtual photon and Z^0 exchange and is effectively the ratio of weak to electromagnetic interactions between the target and electrons. Within the quark-parton model it is directly sensitive to the ratios of quark flavors, and so is independent of the size of the flavor-independent EMC effect. Such a measurement is cleanly interpretable with minimal model dependence and offers the best direct access with available experimental techniques.

We propose to measure the parity-violating asymmetry $A_{\rm PV}$ from ^{48}Ca using 11 GeV beam at 80 μA and the SoLID detector in its PVDIS configuration; the only change from the PVDIS running conditions is the use of a ^{48}Ca target. With 66 days of data taking, we will obtain 0.7-1.3% statistical precision for $0.2 < x < 0.7$ with a 0.7% systematic error. Based on the prominent CBT (Cloet-Bentz-Thomas) model of medium modification [1, 2], this would provide a measurement of the flavor dependence at better than the 6σ level, and has the precision needed to differentiate between models that predict larger or smaller flavor dependence. While such models provide useful guidance in the required precision for a significant experiment, the goal is not to test specific models, but to make a first measurement of the completely unknown flavor dependence of the EMC effect.

A previous version of this proposal (PR12-16-006) was deferred by PAC44 which noted the cost of the ^{48}Ca target, concerns about the radiation associated with the run, and the fact that experiment E12-10-008 [3] will measure the EMC effect on ^{40}Ca and ^{48}Ca, providing an alternative way to look for flavor-dependent contributions to the EMC effect. Since then, there has been a great deal of activity around trying to identify reliable experimental tests of flavor dependence and to evaluate their impact on other measurements, highlighting the importance of understanding whether or not there is a flavor dependence to the EMC effect. It has also led to re-examinations of existing inclusive data, demonstrating that the sensitivity of conventional EMC effect measurements to flavor-dependent contributions is small (as summarized in Sec. 2 and described in detail in Sec. 4.4). In addition, other measurements that have been proposed as a way to look for flavor dependence have been further studied and shown to have insufficient sensitivity (Sec. 4.4). As such, we believe that no other measurement currently planned or under discussion can provide the sensitivity proposed by this measurement. To address the other concerns raised, we have updated the target design to significantly reduce the amount of target material needed, and provided additional detail on the radiation in the hall and at the site boundary, including comparisons to real measurements from the recently-completed CREX experiment. A more detailed summary of the changes relative to the PAC44 submission is included in Sec. 2.

2 Key updates relative to PAC44 submission

The overall goals and general methods of this proposal are much the same as the previous version which was submitted to PAC44. The previous proposal was deferred, noting the cost of a new ^{48}Ca target, the radiation associated with running on calcium, and the fact that experiment E12-10-008 [3] will compare inclusive DIS from ^{48}Ca and ^{40}Ca. We provide here a brief summary of updates that address these issues.

1. Calcium-48 target: Working with the target group, we have modified the design of the target in a way that allows the same effective target thickness while cutting the amount of ^{48}Ca needed by 30% or more. This, combined with reuse of the existing calcium, will dramatically reduce the cost of the target. Details in Sec. 5.1.

2. Radiation: We have reevaluated the radiation dose in the hall and at the site boundary using an improved Geant4 simulation and with more input from the Jefferson Lab Radiation Control Group. We believe the radiation dose in the hall and at the boundary will not be an issue for the requested beam time with ^{48}Ca (details provided in the Section 5.5). We expect the radiation rate in the hall and boundary dose to be approximately a factor of two higher for this experiment than for the PVDIS measurement on deuterium. We also note that while the site boundary estimates are about 50 % higher than the CREX estimation, the measured CREX site-boundary dose at the end was significantly below the estimate provided by RADCON. The radiation shielding design for overall SoLID experiment is still in its infancy and dedicated sky-shine shielding will further reduce the site boundary dose.

3. Other measurements: We have provided more detailed projections for the sensitivity of this proposed measurement, the inclusive EMC measurements, as well as evaluating other options for extractions of the flavor dependence of the EMC effect. These are provided in detail in Secs 4.4 and summarized below.

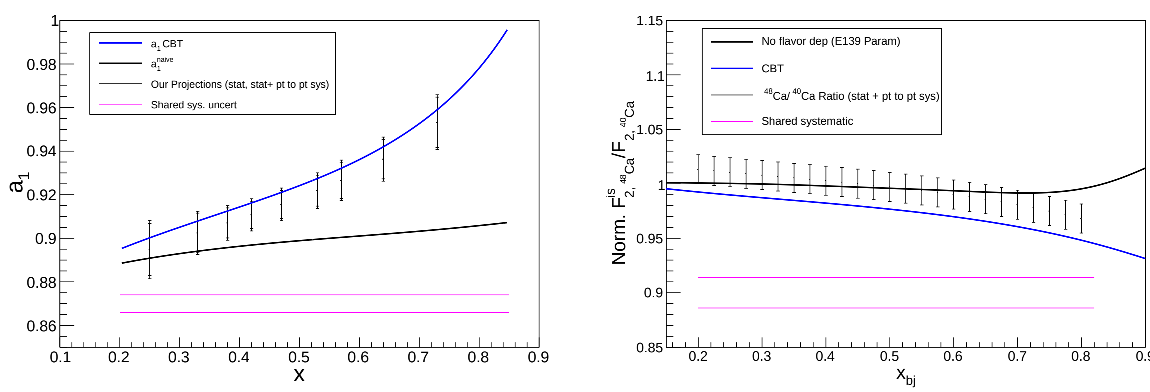

Figure 1: A comparison between the measurements proposed here (left) and the planned E12-10-008 ^{48}Ca/^{40}Ca ratios (right) [3]. The solid black curves are the predictions for no flavor dependence, the solid blue curves are the prediction based on the CBT model [1, 2]. The points show the projected point-to-point uncertainties, based on the CBT prediction, but *shifted towards the null result by 1.5 times the normalization uncertainty* to illustrate the sensitivity to the normalization uncertainty.

Figure 1 shows a direct comparison of the projected results for the parity-violating measurement of a_1 (defined in Sec. 3.1) and the inclusive ^{48}Ca/^{40}Ca ratio of the cross section per nucleon [3]. The black curves represent the null hypothesis (no flavor dependence), and the blue curves represent the predication of the CBT model [1, 2] (detailed in Sec. 4.4.1). To show the importance of the normalization uncertainties, the projected data points are generated based on the CBT model but shifted by 1.5 times the normalization uncertainty. It is clear that the large normalization uncertainty in the cross section ratios makes it difficult to cleanly observe even a relatively large flavor dependence. Note that the uncertainties for the calcium structure function ratios do not account for the model dependence in extrapolating from ^{40}Ca to ^{48}Ca in the absence of any flavor dependence or for the isoscalar correction required for ^{48}Ca. Similar effects for the PVEMC measurement are smaller and discussed in Sections 6.2.5 and 6.2.6.

Table 1 shows the projected uncertainties and the sensitivity of different analyses to the prediction of the CBT model for both the PVEMC and the EMC measurements. The first projected sensitivity considers only the slope in x of a_1 or the ^{48}Ca/^{40}Ca ratios, relative to the null hypothesis, in order to be independent of normalization uncertainties. The second is based on the normalization of the high-x data relative to the null hypothesis, and finally based on a direct comparison of the full data set to the null hypothesis, allowing for normalization shifts of up to 2σ. The ^{48}Ca/^{40}Ca inclusive cross section ratio (EMC) provides only $\sim 2\sigma$ differentiation between the null hypothesis and a model predicting significant flavor-dependent effects. It has no ability to differentiate between the larger effect from the CBT model 4.2.1 and the smallest effect based on the models presented in Sec. 4.2.3. The details of the sensitivity analyses is given in Sections 4.3 and 4.4.1.

	PVEMC (this proposal)	EMC E12-10-008
Uncertainties		
Statistics	0.7-1.3%	0.8-1.1%
Systematics	0.5-0.7%	0.7%
Normalization	0.4%	1.4%
Projected Sensitivity to CBT flavor dependence		
slope in x	3.7σ	2.0σ
high-x values	5.5σ	2.1σ
data vs. null hypothesis	6.2σ	$<2\sigma$
min vs. max flavor dependence	4.4σ	N/A

Table 1: Summary of uncertainties on the projected measurements and significance of the signal comparing the CBT model [1, 4] to no flavor dependence (null hypothesis). "x-dependence" is given as the slope in a_1 or the calcium cross section ratios (in the "EMC region", $0.3 < x < 0.7$, for the cross section ratios). Min. vs max. flavor dependence refers to the range of models considered in Sec. 4.2. Note that the "data vs. null hypothesis" result represents the full sensitivity of the data; the slope and high-x offset are shown mainly to demonstrate the impact of the normalization vs. the point-to-point uncertainties.

While E12-10-008 is scheduled to run in the near future, we believe that it is appropriate to resubmit at this time. The question of the flavor dependence of the EMC effect has been an extremely important and active topic over the past few years years [5, 6, 7, 8, 9, 10, 11], and has potential impact on a wide range of measurements at Jefferson Lab, Fermilab, and a future EIC (as detailed in Sec. 3.4). A measurement of the flavor-dependence provides unique input on the underlying physics of the EMC effect, and can provide insight on the EMC-SRC connection which has become an important part of the JLab 12 GeV program. It is clear that the inclusive measurements have only very limited sensitivity to the flavor dependence [12, 8], and a detailed examination shows that the E12-10-008 measurement cannot provide 3σ evidence for a flavor-dependent EMC effect unless the effect is significantly larger than any of the models we have considered. As such, the measurement utilizing parity-violating electron scattering will be critical to understanding flavor dependence in nuclei no matter what is observed in the ^{48}Ca/^{40}Ca ratios.

3 Introduction

Within QCD we describe the structure of protons and neutrons in terms of their underlying quark and gluon degrees of freedom. Protons and neutrons are also the basic building blocks of more complex systems (nuclei) and this transition between QCD and nuclear physics is still out of reach for modern theory. The effective theories we have for the description of inter-nucleon interactions have been widely successful in producing detailed descriptions of systems such as nuclear structure and scattering processes. However, they are based around the concept that nucleons in the nuclear environment strongly maintain their identities and have few, if any, provisions for how they change.

An open and important question for hadronic physics today is how protons and neutrons are modified when they are bound in a nucleus and how one makes the transition between traditional nuclear physics to QCD. The observation of the "EMC effect", the depletion of the nuclear quark distributions for $0.3 < x < 0.8$ relative to the expectation from nucleon pdfs plus Fermi motion, provides clear evidence that the nuclear pdfs are not simply the sum of the pdfs of unmodified proton and neutrons [13, 14, 15]. But despite this direct measurement of such modification, the underlying physics mechanism(s) for it is not well understood.

While the existence of nuclear modification of the pdfs is well established, important questions remain about the nature of the modification: a detailed description of its A dependence is not yet complete, and we have almost no experimental information on the spin- and flavor-dependence. An improved understanding of these questions will be enormously important in guiding a theoretical understanding, but it is also a pressing experimental issue with broad implications. Without an understanding of the behavior in light nuclei, we rely on models of the modification in the deuteron and ^{3}He in extracting free neutron structure from "effectively free" neutrons in these light nuclei. With no understanding of the flavor dependence, electron- and neutrino-nucleus scattering and nucleus-nucleus collisions assume flavor-independent modification to the pdfs. In electron-nucleus scattering, neglecting potential flavor dependence can impact studies of the A dependence for non-isoscalar nuclei, and yield unknown corrections to DIS and SIDIS measurements from polarized ^{3}He targets. It can have similar impact on neutrino-nucleus scattering, Drell-Yan measurements, high-energy nucleus-nucleus collisions, and for future EIC measurements.

The flavor dependence of the EMC effect has received a great deal of attention in recent years [16, 17, 5, 7, 8], with calculations that examine the flavor and spin dependence of the EMC effect, including some which indicate significant flavor dependence in non-isoscalar nuclei [1, 4]. In addition, the observation of the correlation between the EMC effect and short-range correlations (SRCs) [18, 19, 20] combined with the known isospin structure of SRCs suggest an alternative mechanism for generating such a flavor dependence. While there are now many reasons to believe that the EMC effect should differ for up- and down-quarks in non-isoscalar nuclei, there is essentially no experimental evidence that supports this hypothesis. As such, it is critical to have a measurement that can cleanly isolate the flavor dependence of the EMC effect, independent of other nuclear effects, and with the precision to quantify the flavor dependence as input to parameterization of the EMC effect and to guide detailed calculations of the underlying physics.

One of the primary goals of Jefferson Lab is to study nuclear modification and to study how one can relate the basic QCD degrees of freedom, quarks and gluons, to the objects that nature most readily presents to us, nucleons and nuclei, through the use of the well-understood electron probes. With the 12 GeV upgrade, we will have unprecedented access to the valence quark kinematic region allowing for new constraints on modification. By far, most of the data available on parton distributions is through electromagnetic scattering, which is heavily weighted to the the u-quark distributions and is only sensitive to one particular linear combination of quarks. Parity-violating deep inelastic scattering with leptonic probes provides a powerful method to access *flavor ratios* of quark distributions that have not been as well explored and offers opportunities to study difficult-to-obtain flavor dependent effects within nuclear modification.

The scattering cross section for weak neutral currents is dependent on both the amplitudes for the exchanged virtual photon and neutral Z boson, which interfere to give

$$\sigma \propto |A_\gamma + A_Z|^2 . \tag{1}$$

For $Q^2 \ll M_Z$, the dominant term for the scattering rates is $|A_\gamma|^2$ and for the parity-violating component, the interference term $|A_\gamma^* A_Z|$. One can then form a parity-violating quantity which is the ratio of these two terms, and is measured by the differences between left and right-handed polarized lepton cross sections

$$A_{\rm PV} = \frac{\sigma_R - \sigma_L}{\sigma_R + \sigma_L} \sim \frac{|A_\gamma^* A_Z|}{|A_\gamma|^2}. \tag{2}$$

This asymmetry provides a particularly sensitive method to obtain flavor-dependent effects in nuclear modification as it is a ratio of the weak-to-electromagnetic interactions, which gives access to ratios of quark distributions.

3.1 Deep Inelastic Scattering and PDFs from Electromagnetic and Electroweak scattering

Deep inelastic scattering has provided one of the most important tools in understanding modern hadronic structure. From studying this scattering process we have some of our best evidence for the concepts of quarks as strongly interacting, point-like spin-1/2 objects, the running of the strong coupling constant α_s, and the validity of perturbative QCD, and confinement. It has been used for decades as a tool to map nucleon structure through parton distribution functions (PDFs) for which we have no predictions from first principles. The universality of these parton distribution functions is absolutely critical in our modern studies of deep inelastic neutrino scattering and of high-energy physics at facilities like the RHIC and the Large Hadron Collider.

At sufficiently large momentum and energy transfer from an electromagnetic probe to a hadronic target, a transition takes place where the underlying QCD degrees of freedom are exposed and the target appears as an incoherent sum of weakly interacting partons which we identify as quarks. The differential cross section for the electromagnetic scattering interaction can be written in the lab frame as

$$\frac{d^2\sigma}{d\Omega dE'} = \frac{4\alpha E'^2}{Q^4} \cos^2\frac{\theta}{2} \left(\frac{F_2(x,Q^2)}{\nu} + \frac{2F_1(x,Q^2)}{M} \tan^2\frac{\theta}{2} \right) \tag{3}$$

where α is the fine structure constant, Q^2 is the negative of the four-momentum transfer, E and E' are the initial and final probe energies, $\nu = E - E'$, M is the nucleon mass, and F_1 and F_2 are the quark-parton structure functions with x, the Björken scaling variable,

$$x = \frac{Q^2}{2M\nu}, \tag{4}$$

F_2 is expressed in terms of the quark and anti-quark parton distribution functions

$$F_2(x,Q^2) = x \sum_q e_q^2 \left(q(x,Q^2) + \bar{q}(x,Q^2) \right), \tag{5}$$

where e_q are the quark charges. This scaling variable has the interpretation of the fraction of momentum carried by that quark when the nucleon is boosted to the speed of light. The parton distribution functions $q(x,Q^2)$ carry the soft, non-perturbative nucleon structure and represent the probability that the quark carries that fraction of momentum x. The Q^2 dependence is predominantly logarithmic which is successfully predicted within the framework of perturbative QCD where it is order-by-order identified with phenomena such as soft gluon emission. Related to F_2 is F_1 through the longitudinal structure function $F_L = F_2 - 2xF_1$.

Equating $F_L = 0$ is the Callan-Gross relation and represents treating the partons as free, point-like spin-1/2 objects.

One challenge in this framework is accessing the quark flavors since the interaction is only sensitive to the charge-squared-weighted sum of the parton distributions, and therefore most heavily to the u-quarks. Exploiting charge symmetry between protons and neutrons, the idea that the u and d-quark distributions are symmetric between the two, and suppressing the sea quark contributions through studies at high x, a deconvolution can be performed. However, since there are no sufficiently high luminosity free neutron targets, neutrons are typically studied bound in a nucleus such as deuterium. How representative such a target is to the free neutron beyond simple binding effects is an open question, but deuterium measurements remain a standard in extracting neutron physics.

A method of accessing quark flavor information without having to consider such binding effects is through parity-violating processes which measure weak force couplings to the quarks. For now we assume the Callan-Gross relation and $Q^2 \gg M^2x^2$; the full framework is presented in Appendix A. In the quark-parton model, the left-right polarized lepton scattering asymmetry given in Eq. 2 can be expressed in terms of the parton distribution functions by

$$\frac{\sigma_R - \sigma_L}{\sigma_R + \sigma_L} = A_{\rm PV} = -\frac{G_F Q^2}{4\sqrt{2}\pi\alpha}\left[Y_1 a_1(x) + Y_3(y) a_3(x)\right], \tag{6}$$

where G_F is the Fermi constant and

$$Y_1 \approx 1 \;\; ; \;\; Y_3(y) \approx \frac{1-(1-y)^2}{1+(1-y)^2} \tag{7}$$

with

$$a_1(x) = g_A^e \frac{F_1^{\gamma Z}}{F_1^{\gamma}} = 2\frac{\sum_i C_{1i} e_i (q_i + \bar{q}_i)}{\sum_i e_i^2 (q_i + \bar{q}_i)} \;\; ; \;\; a_3(x) = g_V^e \frac{F_3^{\gamma Z}}{2F_1^{\gamma}} = 2\frac{\sum_i C_{2i} e_i (q_i - \bar{q}_i)}{\sum_i e_i^2 (q_i + \bar{q}_i)}. \tag{8}$$

with $y = \nu/E$, g_A^e and g_V^e the axial and vector couplings to the electron respectively, and C_{1i} and C_{2i} the effective quark couplings dependent on the weak-mixing angle $\sin^2\theta_W$. In practice the a_1 term dominates the asymmetry as the C_{2i} couplings are suppressed by an order of magnitude relative to C_{1i}.

The power of this method is elucidated when one considers nuclear quark distributions for the light flavors u_A and d_A and expand a_1 about the isoscalar $u_A = d_A$ limit and at high enough x where the sea quarks do not contribute significantly

$$a_1 \simeq \frac{9}{5} - 4\sin^2\theta_W - \frac{12}{25}\frac{u_A^+ - d_A^+}{u_A^+ + d_A^+} \tag{9}$$

with the convention that $q^{\pm} = q(x) \pm \bar{q}(x)$. Parity-violating deep inelastic asymmetry measurements are therefore directly sensitive to differences in the quark flavors. In turn, for isoscalar targets (and neglecting sea quarks) a_1 roughly becomes a constant and the measurement becomes a test for charge symmetry violation [21].

3.2 Nuclear PDF Modification and the EMC effect

The EMC effect, first reported by the European Muon Collaboration collaboration [22] almost 40 years ago, provided the first direct evidence that the quark distributions in nucleons bound in a nucleus are significantly different from those of free nucleons. This was demonstrated by observing a difference in the ratios of deep-inelastic muon scattering cross sections between a heavy nucleus (in this case iron) and deuterium. They showed that this ratio deviated from a simple constant expectation across a range of x, as confirmed for a range of nuclei at SLAC [23] and JLab [18], as shown in Fig. 2. To compare between nuclei where $N \neq Z$, a model-dependent "isoscalar" correction is made to the interaction cross section to account for an excess of neutrons, typically assuming that the free nucleon structure functions can be used to correct for presence of excess neutrons in nuclei.

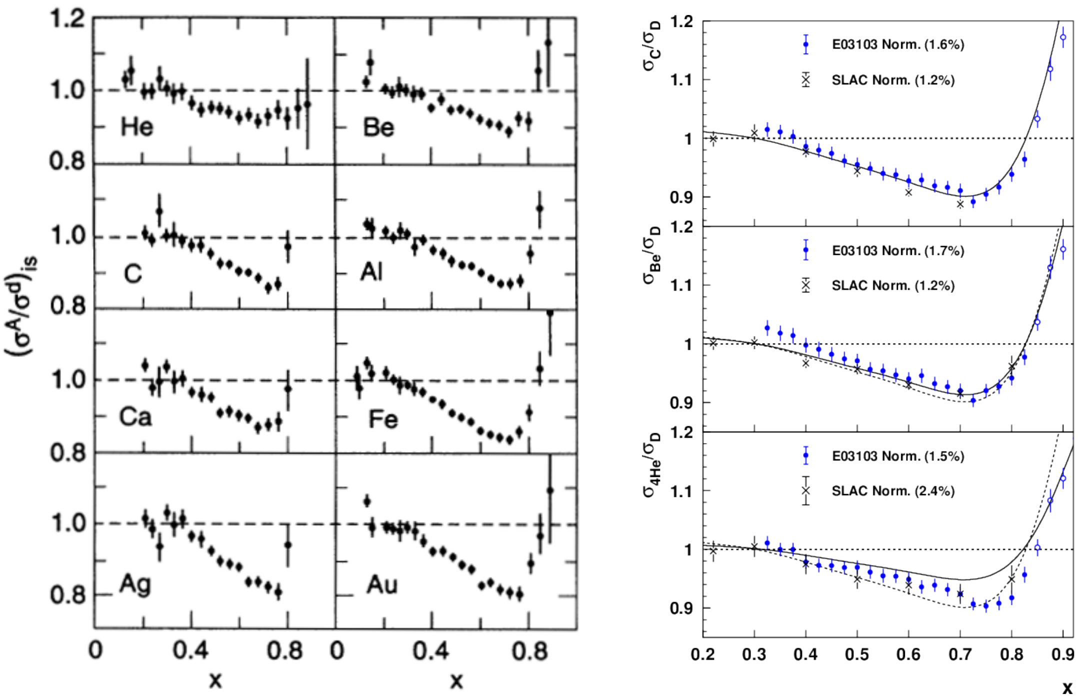

Figure 2: Data demonstrating the EMC effect for a range of nuclei from SLAC E139 [23] (left plot) and JLab E03-013 [18] (right plot).

Prior to JLab experiments, the large-x EMC ratios, $(\sigma_A/A)/(\sigma_D/D)$, where σ_A has been corrected for neutron excess, for various nuclei showed the following features,

- an enhancement attributed to Fermi motion for $x > 0.9$,
- a suppression in the range $0.3 < x < 0.8$, dubbed the "EMC effect", with a minimum around $x = 0.7$
- a universal x dependence in the EMC region, with the size of the suppression slowly increasing with A (scaling as the average nuclear density)

Fermi motion gives a strong enhancement to the nuclear structure function for $x > 0.8$ due to the enhanced impact of smearing caused by nucleon motion at large x, where the nucleon pdfs are going rapidly to zero. We focus here on the "EMC region", generally taken to be $0.3 < x < 0.7$. Shortly after the data was obtained, it became clear that Fermi motion alone was insufficient to explain the effect. Despite decades of work there is still no commonly-accepted explanation for the EMC effect; we refer the reader to the following reviews [13, 14, 15].

In the last decade or so, Jefferson Lab has provided important new data that has modified our understanding of the EMC effect. First, measurements of the EMC effect in light nuclei [18] demonstrated that the EMC effect does simply scale with nuclear density, as ^{9}Be shows roughly the same EMC effect as ^{4}He and ^{12}C, despite having an extremely low average nuclear density. It was initially suggested that this surprising result was related to the significant cluster structure in ^{9}Be, which has a significant component with two alpha particles and an extra neutron. While the average nuclear density is low, most of the nucleons (and all of the protons) are in dense, alpha-like clusters, and so their local environment is a dense cluster.

A short time later, the same nuclear dependence was observed in the contribution of Short-Range Correlations (SRCs) in light nuclei [19], with ^{9}Be having a greater contribution from SRCs than expected based on conventional models where the contribution scaled with the nuclear density. SRCs are pairs of nucleons with large relative momentum generated by interaction via the strong short-range components of the NN interaction. As such, it was natural that the contribution of SRCs would relate to the number of nucleons that are extremely close together, and therefore also be enhanced due to the strong alpha clustering in ^{9}Be. In this 'local density' picture initially used to describe the EMC ratios for light nuclei, both the the EMC effect and presence of SRCs are the result of configurations with nucleons very close together. However, the correlation between the observed EMC effect and number of SRCs for various light and heavy nuclei also suggested another possibility [20], that the EMC effect was directly generated by the presence of the high-momentum pairs of nucleons in the SRC, with the nucleon modification driven by large off-shell effects in these highly-virtual configurations. Because of the isospin structure of SRCs, which are strongly dominated by np pairs [24, 17, 25], minority nucleons will spend a larger fraction of their time at extremely large momenta, which would translate to an enhanced EMC effect for these nucleons in a picture where the EMC effect is driven by off-shell effects. It is interesting to note that recent calculations that include a flavor dependence to the EMC effect [1, 4], and a range of scaling models based on the idea of the EMC effect being driven by local density or high virtuality [5] all agree that the EMC effect is enhanced in the minority nucleons, although the size of the isospin dependence varies by about a factor of two.

Historically, explanations of the EMC effect have neglected the potential impact of flavor-dependent effects, and many have neglected the impact of detailed nuclear structure, focusing on effects which have simple scaling behavior with nuclear mass or density [23, 13, 14]. Recent measurements of the EMC effect in light nuclei [18] have made it clear that a complete understanding of nuclear PDFs requires a detailed understanding of the connection between the nuclear effects and details of the nuclear structure. It is also clear that our understanding of the EMC effect will not be complete without an understanding of the flavor-dependence of the nuclear modification to PDFs. As noted above, the data for heavier nuclei show a slow increase in the nuclear modification as A increases. While heavier nuclei have $N > Z$, and are in principle sensitive to both the overall A dependence and any flavor-dependent effects, there is a strong correlation between A and N/Z for heavier nuclei, making it difficult to disentangle A-dependent effects from any flavor dependence. The Particle Data Group states in their 2013 review of the electroweak model that *"it would be important to verify and quantify this kind of effect experimentally, e.g., in polarized electron scattering."* [26]

While a flavor-dependent effect is challenging to study in conventional measurements of the EMC effect, as discussed in the following section, the flavor sensitivity of parity-violating electron scattering provides an ideal probe of such effects. The parity-violating asymmetry in deep inelastic scattering provides direct access to flavor dependence in the EMC effect, cleanly separated from flavor-independent nuclear modification of the PDFs.

3.3 Possible Indications of Flavor Dependence

Most models and parameterizations of nuclear PDFs do not include flavor-dependent medium modification, and so any true flavor dependence in neutron-rich nuclei is absorbed into the parameterization of the A dependence. This can have an important impact on any measurement where the flavor sensitivity differs from direct measurements of the nuclear PDFs. Measurements involving weak coupling to the nuclear quark distributions will have a different contribution from up and down quarks, and a flavor-independent modification of the nucleon PDFs will not yield the correct result. Similarly, nuclei with unusual N/Z ratios will not be well represented by conventional parameterizations of the EMC effect. For most nuclei, the A-dependent parameterizations of the EMC effect will be fairly reliable, as nuclei in a given mass region tend to have a relatively narrow range of N/Z values. However, a difference between the EMC effect for up-quark and down-quark distributions could change the nuclear effects in ^{3}H or ^{48}Ca from those observed in ^{3}He or ^{40}Ca.

In light of the importance of such an effect, several avenues should be explored and by using data from multiple techniques, a more complete picture can emerge. While we discuss several possibilities, we stress that the parity-violating technique presented here offers one of the most direct, precise, and theoretically clean access to these observables and would serve as the strong underlying foundation for all of these studies. In this section, we present observables that are sensitive to a flavor dependent EMC effect, and have been discussed as potential signatures for such an effect. However, while these observables are clearly impacted by flavor dependence, none of them provide clear or direct evidence for a flavor dependent EMC effect.

3.3.1 The "NuTeV Anomoly"

The NuTeV experiment [27] at Fermilab was designed as a measurement of the electroweak mixing angle $\sin^2\theta_W$ through neutrino deep inelastic scattering measuring together charged and neutral current neutrino and anti-neutrino scattering. With those cross sections, one can measure the weak mixing angle using the Pachos-Wolfenstein relation [28],

$$R_{\rm PW} \equiv \frac{\sigma(\nu_\mu N \to \nu_\mu X) - \sigma(\bar{\nu}_\mu N \to \bar{\nu}_\mu X)}{\sigma(\nu_\mu N \to \mu^- X) - \sigma(\bar{\nu}_\mu N \to \mu^+ X)}. \tag{10}$$

which reduces to $\frac{1}{2} - \sin^2\theta_W$ in the case of an isoscalar target and the absence of charge symmetry violation. This quantity is particularly attractive to study as a large number of systematic uncertainties cancel, including a great deal of nuclear structure. However, important corrections must be made in the case where there is an excess of neutrons which is the case for heavy nuclei typically used as targets in neutrino experiments.

For NuTeV, high purity ν and $\bar{\nu}$ beams from the decay of charged pions or kaons were produced by the Tevatron and the neutrino interactions were detected 1.5 km downstream in a large detector array. This array consisted of steel-scintillator target calorimeter followed by an iron-toroid spectrometer. The published result on $\sin^2\theta_W$ was approximately 3σ from the standard model prediction, Fig. 3 and has caused a significant amount of discussion in the community regarding the discrepancy [29].

A large class of possible explanations has been generated involving unconsidered corrections in the NuTeV analysis, including higher order QCD evolution, a strange sea asymmetry, charge symmetry violation, nuclear shadowing, or a flavor-dependent EMC effect. A calculation of the isovector EMC effect by Cloët *et al.* [1, 4], which we discuss in Sec. 4.2.1, is shown in Fig. 4. In this model, a flavor dependence modifies the nuclear u- and d-quarks differently within the iron nucleus, irrespective of the nucleon in which they are bound, by the mean isovector field from the surrounding nucleus. This model can account for 2/3 of the observed difference, resolving the discrepancy and leaving significantly less room for additional corrections.

While this demonstrates the importance of understanding the flavor structure of the target in the NuTeV measurement, the fact that many different ways to resolve the discrepancy have been proposed makes it difficult to treat this as a strong indication of a flavor-dependent EMC effect without additional data to support this particular explanation. At the same time, without quantification of the flavor dependence of the EMC effect, which must be there at some level, we do not have a quantitative understanding of what additional effects would be required to resolve the NuTeV anomaly.

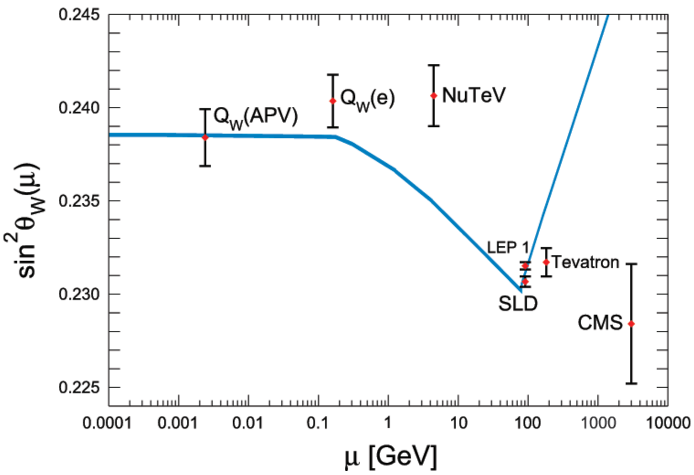

Figure 3: Constraining world data on the running of $\sin^2\theta_W$ including the published NuTeV result [27].

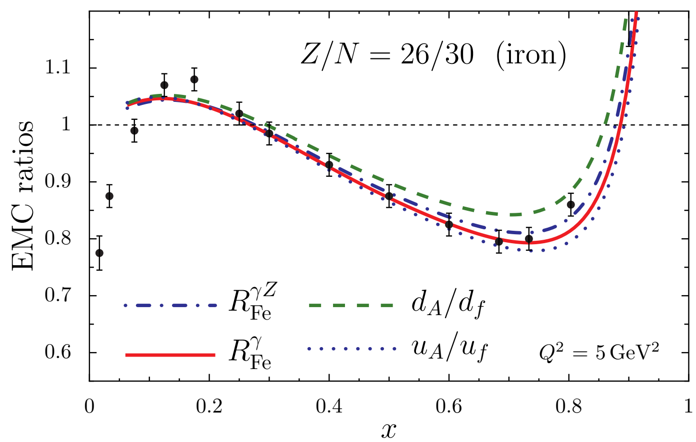

Figure 4: Isovector parton distribution modification in Fe from Cloët *et al.* [4]. The dashed and dotted lines show the modification for d and u quarks, respectively, and the solid and dashed lines show the ratio of nuclear pdfs to proton plus neutron in electron scattering and for the $\gamma - Z$ interference contribution.

3.3.2 The EMC-SRC connection

As noted in Sec. 3.2, the observed correlation between the EMC effect and the strength of Short-Range Correlations (SRCs) in nuclei led to the question of whether the isospin structure of SRCs, where minority nucleons are more likely to be part of an SRC, translates into an enhanced EMC effect for these minority nucleons [20, 17]. This typically assumed that the large-momenta associated with the SRCs is the source of the EMC effect through the off-shell corrections in these Highly Virtual (HV) configurations. In this case, the isospin structure of SRCs would drive a similar structure in the EMC effect. Another explanation for the similar behavior in the EMC effect and SRCs was based on the idea that the modification occurs within short-distance configurations (as opposed to high-momentum configurations), and the probability of nucleons being very close together drives both the EMC effect (through nucleon overlap) and the generation of SRCs (associated with the short-distance part of the NN potential). In this case, both effects are driven by the local density (LD) as seen by the nucleons in the nucleus, which does not necessarily imply an isospin dependence in the EMC effect [17].

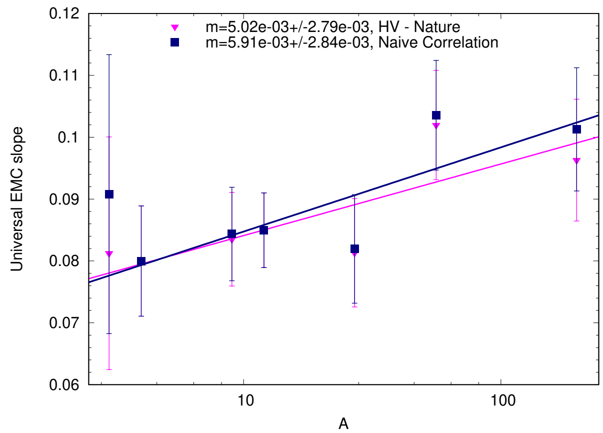

Figure 5: The slope of the ”universal EMC effect” vs A, based on the analysis of Ref. [7] (”HV - Nature”), and the naive (flavor-independent) result where the EMC slope is scaled down by a factor of a_2, the relative SRC contribution in heavy nuclei compared to the deuteron.

Examinations of the quality of scaling between the EMC effect and SRCs [12] slightly favor the flavor-independent LD hypothesis over the flavor-dependent HV model, but only at the 2σ level, and with some model dependence in the comparison. A more recent examination found that assuming the HV picture yielded a universal EMC effect per deuteron [7], consistent with the idea that the SRCs drive the EMC effect. However, a later examination [8] showed that the same was true under the flavor-independent LD assumption, and the LD picture gave a somewhat better description of the data.

Existing measurements of the EMC effect in non-isoscalar nuclei have limited direct sensitivity to the flavor dependence of the EMC effect, as illustrated in Fig. 5. The figure shows the universal EMC slope from the HV approach of Ref. [7] (“HV-Nature”) to that obtained from the most naive analysis of the correlation (“Naive Correlation”). In the naive correlation analysis, the EMC effect is assumed to scale with a_2 (the relative contribution of SRCs in the heavy nucleus compared to the deuteron), neglecting any isospin structure of the SRCs (and thus flavor-dependence in the EMC effect). The two models, one with explicit flavor dependence and one without, are identical for isoscalar nuclei and show only small differences for non-isoscalar nuclei, below 0.5σ for even the most neutron-rich nucleus (Au).

Because the impact of an explicit flavor dependence on the inclusive EMC effect is small, it is difficult to use such measurements to provide meaningful constraints. Section 4.4.1 includes a detailed evaluation of the sensitivity of a direct comparison of ^{48}Ca to ^{40}Ca and shows that such a comparison, while more sensitive than existing data, will not answer the question of whether or not there is a flavor dependence to the EMC effect.

3.3.3 PDF Fits

There have been several global analyses that have examined the possibility of flavor dependent nuclear effects. Primarily, these analyses have concentrated on the tension between data from neutrino interactions (charged current) and data from charged lepton scattering and Drell-Yan (neutral current) in fits that assume a flavor-independent modification of the light quark distributions in nuclei. An analysis by Schienbein *et al.* [30, 31] noted a striking difference between the nuclear correction factors F_2^A/F_2^D found by fitting charged lepton (neutral current) and Drell-Yan data compared to fitting charged current neutrino scattering data, Fig. 6. In this method, comparisons between “free” nucleon PDFs to the nuclear PDFs are made. Later Kovarik *et al.* [32] performed a global analysis using partitions of the neutrino-nucleus DIS, charged lepton-

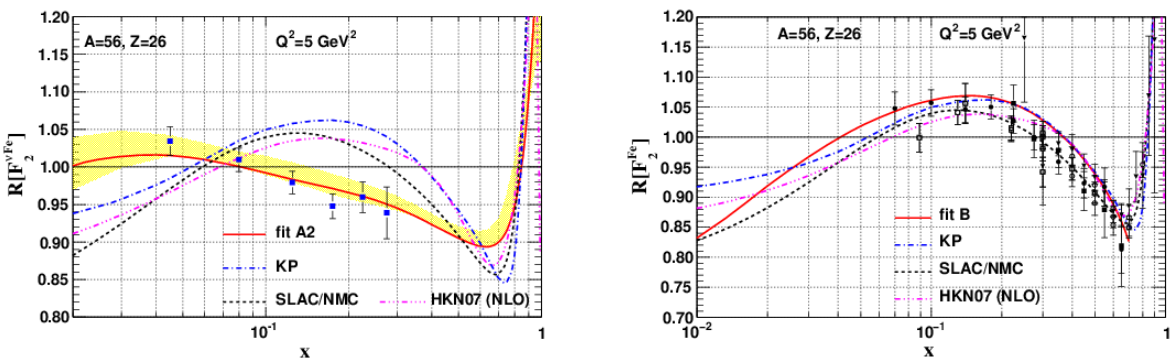

Figure 6: Differences in nuclear correction factors $R = F_2^A/F_2^N$ for charged current neutrinos (left) and neutral current leptons and Drell-Yan (right) at $Q^2 = 5\ \mathrm{GeV}^2$ from [31].

nucleus DIS, and Drell-Yan data to test the compatibility between these data sets. In the Kovarik "nCTEQ" analysis, a goodness of fit test is used while varying the contribution weights between the set of neutral current (lepton and Drell-Yan) data and charged current the neutrino data. In those two partitions, they find no compromise fit that has acceptable χ^2/NDoF simultaneously for both sets at the 90% confidence level. Furthermore, individual data sets from the NuTeV neutrino iron results and from lepton-Fe exceed the 99% limit in the compromise fits.

This result contrasts one by de Florian *et al.* [33] which was a global fit where the nuclear effects are parameterized and included in the fit. In that analysis they claim compatible fits within their errors between all data and cites possible differences in the overall deuterium normalization (Kovarik calculates the deuterium from free PDFs, rather than use the sparse neutrino data) or possibly "disregarded uncertainties" and "theoretical ambiguities". While the de Florian analysis included neutral and charged pion production data from RHIC as well, the χ^2/dof for these additional data sets do not appear anonymously large. An analysis by Paukkunen *et al.* [34] notes that only the NuTeV neutrino data and data from CHORUS (lead), CDSHW (iron), and the NuTeV antineutrino data show no controversy. Later they argue [35] that unnoticed fluctuations in the overall normalization to the NuTeV data are sufficiently large to cause tension.

A review of these issues is given in Ref. [36], Section 8. There they suggest that when the full uncertainties for all the measurements are taken in quadrature, as in the de Florian fit, the discriminating power for tension may be reduced. The amount of controversy and uncertainty demands measurements such as this proposal which could unambiguously address the situation. All of these investigations assumed that charge symmetry between the neutron and proton held.

3.3.4 SIDIS

Semi-inclusive deep inelastic scattering provides access to quark flavors with an electromagnetic probe by tagging pions in the final state of the reaction. Such methods rely on factorization in which the hadronization process is decoupled from the initial parton distributions. A super-ratio of π^-/π^+ between deuterium and an asymmetric nuclear target would be sensitive to variations in the flavors after a correction for differences between π^+ and π^- hadron attenuation effects in the nuclear environment. Constraining all possible hadronic and electromagnetic effects as one goes to large A and Z to sufficient precision is the primary challenge. Uncertainties in nuclear effects (including Coulomb effects) for π^+ and π^- production, challenges in obtaining complete kinematic coverage, and the requirement for demonstration of independent fragmentation

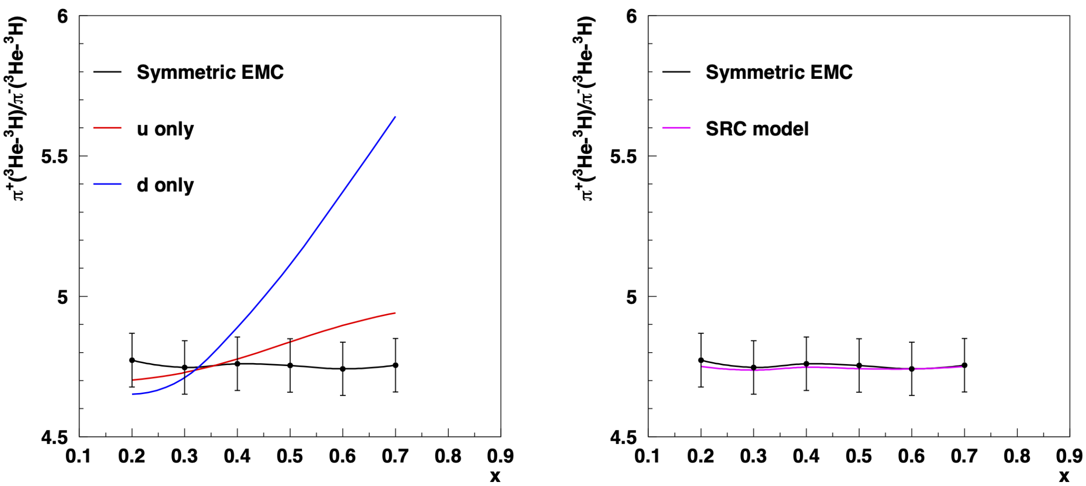

Figure 7: Projected impact of flavor dependence of the EMC effect on the comparison of π^+ and π^- production from ^{3}H and ^{3}He. The left panel shows the prediction from a flavor-independent EMC effect (black curve) compared to the an extreme projection assuming that the EMC effect is carried entirely by the up (red curve) or down (blue curve) quarks in the nucleus (This is the most sensitive of the variables considered the CLAS tritium-target LoI. [38]). The right panel shows the same observable assuming the flavor dependence based on Ref. [7] (magenta curve), indicating no sensitivity in this more realistic flavor dependence. In this particular model, neither this nor the other observables studied in [38] allow for a meaningful test of the flavor dependence.

to high precision led to the deferral of a previous proposal to examine the flavor dependence of the EMC effect in SIDS from heavy nuclei [37].

A Letter of Intent for CLAS [38] examined the possibility of making such a measurement via the comparison of π^+ and π^- production in ^{3}H and ^{3}He. In this measurement, nuclear effects are smaller and the comparison of π^+/π^- production in ^{3}H and ^{3}He would cancel additional systematic effects. While the CBT calculation uses a mean-field approach and cannot provide reliable predictions for A=3 nuclei, estimates based on extreme models of flavor dependence (EMC effect coming entirely from down quarks) showed a observable signal of flavor dependence (left panel of Figure 7). However, this extreme assumption is inconsistent with all of the models we discuss in Sec. 4.2, for which the proton (or up-quark) EMC effect would be enhanced in ^{3}H and suppressed in ^{3}He. An updated estimate, assuming a realistic EMC effect where the proton EMC effect is twice that of the neutron for ^{3}H (and half for ^{3}He), yields a near-total cancellation between the effects in ^{3}H and ^{3}He, as shown in the right panel of Fig. 7.

3.3.5 Drell-Yan

Drell-Yan measurements offer access to complementary data from DIS probes as they are sensitive to the flavors through the annihilation of sea quarks with the valence quarks of a heavy target. In particular, for pionic Drell-Yan the production ratios of $\pi^- A/\pi^- D$ would have cancellation in the pion quark distributions, which are not as well known. Because of the valence $\bar{u}$ in the π^- and the charged-squared weighting of the cross section, the π^- ratio is particularly sensitive to the u-quark EMC effect. Similarly, but without the benefit of the charge-squared weighting, the π^- ratio shows sensitivity to the d-quark effects. As pre-

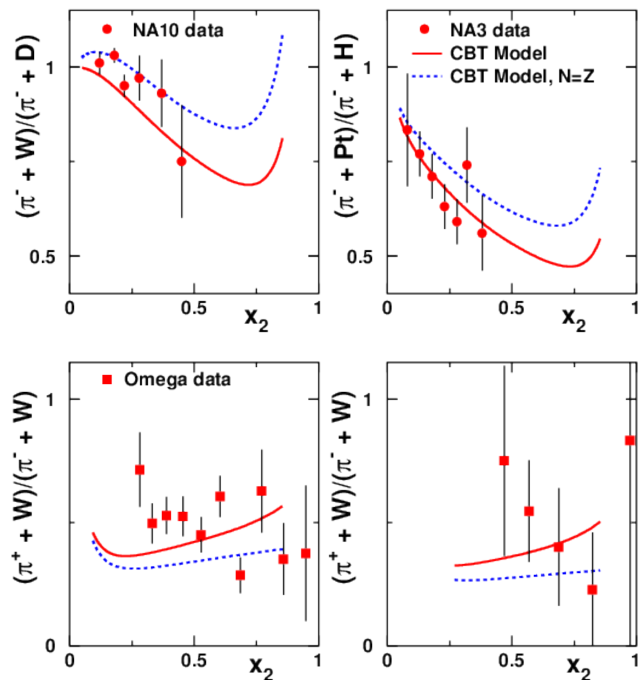

Figure 8: Existing pionic Drell-Yan data for ratios of heavy target to deuterium data compared to the CBT model [16]. A slight preference is shown for the CBT model, but is not conclusive.

sented by Dutta *et al.* [16], within the CBT model there is a slight preference in existing pionic Drell-Yan measurements to support such an effect over the $N = Z$ predictions, but is not statistically strong, Fig. 8.

The AMBER (formerly COMPASS-II) [39, 40] experiment has proposed measuring the π-induced Drell-Yan with carbon and tungsten targets. These data will provide a complementary measurement. Specifically, their initial phase is designed to separate valence- and sea-quark contributions to the pion structure by measuring both the π^+ and π^- absolute cross sections on carbon and tungsten targets. AMBER data will cover the range $0.08 \leq x_2 \leq 0.34$. From these, AMBER can investigate the flavor-dependent valence EMC effect. Forming the ratio of $\frac{\sigma^{\pi^+ A}}{\sigma^{\pi^- A}} \approx \frac{1}{4}\frac{d^A}{u^A}$ gives some sensitivity to the flavor dependence of the nuclear EMC effect. Here, "approximately" represents simplifications from leading order, and from ignoring the sea quarks in the proton. With their tungsten target, AMBER's statistical uncertainty will be approximately $\pm 5\%$, which can be compared with the uncertainties from previous measurements shown in Fig 8. AMBER has also proposed to measure the ratio of the difference between π^+ and π^- cross sections on carbon and tungsten targets, i.e. $\frac{\sigma^{\pi^+ C} - \sigma^{\pi^- C}}{\sigma^{\pi^+ W} - \sigma^{\pi^- W}}$, which gives the ratio of the valence distributions, measured to between $\pm 2\%$ and $\pm 5\%$. The ratio $\frac{\sigma^{\pi^- C}}{\sigma^{\pi^- W}} \approx \frac{u^C}{u^W}$ can also be formed with the proposed AMBER data [16].

3.4 Impact of Flavor Dependent Nuclear Corrections on other measurements.

The observables presented in the previous section are sensitive to the presence of flavor dependence and were all, at least at one time, considered potential signatures of a flavor-dependent EMC effect. Without a clear understanding of the flavor dependence of the EMC effect, the interpretation of these data will be uncertain. We provide here additional examples of observables that will be modified in the presence of significant flavor dependent nuclear modification, but which, like the NuTeV anomaly, involve other corrections or uncertainties that are not sufficiently constrained to make these measurements useful as tests of the flavor dependence.

3.4.1 Neutron PDFs

The neutron structure function is often extracted from measurements on the deuteron, with significant corrections to account for the proton contribution, especially at large x values. The neutron can also be extracted from comparisons of ^{3}H and ^{3}He structure functions. In this case, only the difference of the nuclear corrections for these two nuclei enters into the extraction of F_{2n}, and this is directly sensitive to the difference in the nuclear effects for the proton and neutron. Even with the assumption that the proton distributions in ^{3}He are identical to the neutron distributions in ^{3}H, there is a difference in the relative nuclear effects when including only conventional smearing corrections [41]. While this portion of the isospin dependence (and its estimated uncertainty) is accounted for in calculations aimed at extracting F_{2n}/F_{2p} from the ratio of ^{3}He to ^{3}H, additional flavor dependence associated with nuclear effects beyond simple binding and Fermi motion will yield an additional correction. While the main MARATHON analysis [42] assumes that any flavor dependence beyond what is included in the Kulagin and Petti model [43, 44] is negligible, other approaches [45, 46] raise questions about this assumption.

Polarized ^{3}He nuclei are often used as effective polarized neutron targets. The use of such targets in DIS and SIDIS measurements will be sensitive to the flavor dependence of nuclear effects in both the polarized and unpolarized pdfs. As noted above, some models account for the isospin dependence associated with the difference in proton and neutron distributions in the nucleus, but neglect any flavor dependence beyond this.

3.4.2 Nuclear Dependence of the EMC Effect

Measurements of the EMC effect in medium-to-heavy nuclei show that the effect scales approximately as the nuclear density, but the variation is slow and not precisely measured. Above mass 40, all measurements are made on neutron-rich nuclei, with N/Z generally increasing as one goes to heavier nuclei. As such, the observed A dependence of the EMC effect in heavy nuclei represents a combination of the density dependence and the neutron excess, meaning that even a modest flavor dependence could have a noticeable impact on the density dependence extracted assuming flavor-independent correction. While nuclei like Au and Pb have a very large neutron excess and, potentially, a significant flavor dependence, they cannot be compared to isoscalar nuclei of similar mass, only nuclei of similar mass with somewhat different neutron excess. This makes the extraction of the nuclear dependence in heavy nuclei unreliable, and reduces their impact on constraining models of the EMC effect and on extrapolation of nuclear effects to symmetric nuclear matter.

3.5 Summary

The EMC effect is one of the best cases we have for the medium modification of bound nucleons and has been known for over 30 years, but the mechanism is still not well understood. Experimentally, there is considerable room for additional investigation, in particular in the realms of asymmetric nuclei and small flavor differences in the modified quark distributions. There are several hints that the underlying assumption that quark modification is entirely isoscalar in nature may be inconsistent in measurements that would be sensitive to such effects. Parity-violating measurements offer an excellent window in exploring these assumptions.

4 Measurements of the Flavor Dependence of the EMC effect

4.1 Choice of Target

It is clear that a large proton-neutron asymmetry is favorable for such a measurement through PVDIS. An isoscalar target would test for charge symmetry violating terms which are expected to be subdominant to an isovector effect. A measurement has already been approved for deuterium which can test charge symmetry violation through the same technique and will provide precision on the order of 1% up to $x = 0.7$ [47]. If the effects in deuterium turn out to be surprisingly large, an isoscalar measurement on a medium-to-heavy symmetric nucleus such as ^{40}Ca would likely be well motivated.

There are many potential target options with sufficient neutron excess, though very high Z targets present additional complications which must be carefully considered. Our nucleus criteria include

- providing a high fractional neutron excess, $(N - Z)/A$, and relatively large EMC effect;
- minimizing beam radiative corrections which scale as Z^2 while scattering rates only scale with A;
- the size of Coulomb corrections and their impact on the parity-violating asymmetry.

A wide range of nuclei are possible candidates with reasonable values of $(N - Z)/A$ as well as a relatively large EMC effect. ^{9}Be, ^{48}Ca, and ^{208}Pb have $(N - Z)/A$ values of 0.11, 0.17, and 0.21, respectively. ^{9}Be would be expected to have a significantly smaller flavor asymmetry, as well as a somewhat smaller overall EMC effect, although a thicker target could be used. While the light nuclei may be of interest in testing microscopic calculations, such calculations do not yet exist and we focus on heavier nuclei, where the expected effect is larger.

For this experiment, we choose a target of ^{48}Ca due to its advantages over other heavier target. ^{48}Ca has a larger fractional neutron excess than other nuclei of similar mass, and as such is expected to have a larger flavor dependence, as seen in the CBT model [2] (Fig. 9) for which the flavor-dependent effect is half the size in ^{56}Fe compared to ^{48}Ca. For heavier nuclei like ^{208}Pb (or targets like depleted uranium and gold with similar N/Z), the flavor dependence scales roughly as N/A and so is roughly 25% larger then for ^{48}Ca. While this would allow for an equivalent measurement with a factor of roughly 1.5 lower statistics, sufficient rates can be achieved with ^{48}Ca using only a 12% radiator, whereas an equivalent DIS rate in lead would require more than a 60% radiator (40% radiator even if the rate was to be scaled down to yield equivalent sensitivity on ^{208}Pb). The radiative effects contribute non-linearly in the deconvolution scheme due to the rising cross section with lower-energy electrons having undergone radiation. It would also increase the photon and pion rates in the detectors and the radiation generated in the hall.

Coulomb corrections for high-Z targets have often been calculated in the so-called effective momentum approximation [48] and have been shown to be quite successful at lower energies even for targets as heavy as lead in quasielastic scattering [49]. In this approximation, the relative size of the correction is smaller as one goes to higher energy. For a heavy target like lead, a correction factor $V_C \approx 18$ MeV is applied to the incoming electron. V_C for ^{48}Ca is ~ 5 MeV and would have a sub-0.1% effect in this framework. The authors are unaware of calculations that have been carried through the full DWBA including the nuclear weak potentials for DIS.

4.2 Size of the Isovector EMC Effect

Quantitative predictions for the possible size of this effect are sparse, so we must rely on the few estimates available. However, the authors would like to stress that this proposal is to provide a clean and sensitive measurement of flavor-dependent nuclear effects in a sector where measurements have limited sensitivity or significant model dependence, rather than to test specific models. However, such models provide useful guidance in the required precision for a significant experiment.

4.2.1 Cloët-Bentz-Thomas (CBT) model

It was proposed by Cloët *et al.* [1] that one possible resolution to the NuTeV anomaly was through the existence of an isovector EMC effect. Calculations, which we will call the Cloët-Bentz-Thomas (CBT) model, were carried out in the Nambu-Jona-Lasinio Model, which is a chiral effective theory treating the quark interactions as four-point contact interactions and contains important QCD concepts, such as confinement. To produce a nucleon model, the Faddeev equations are solved for a quark-diquark configuration. An isovector mean field is introduced and the free parameters are constrained to reproduce nucleon and nuclear properties such as nucleon masses and the empirical symmetry energy from the Bethe-Weizsäker formula. With these ingredients, quark distributions can be obtained for symmetric and antisymmetric matter.

This type of model has been very successful in reproducing the quark distributions for the EMC effect and the measured structure functions. In Ref. [1], the impact of the flavor-dependent nuclear PDF modification on the NuTeV anomaly was evaluated in the CBT model. The calculation was able to explain two-thirds of the anomaly, suggesting that the size of the flavor-dependent EMC effect predicted in this model is of the correct scale to resolve this long-standing issue.

Later predictions were made within this model specifically for the PVDIS a_1 term for iron and lead [4]. Calculations for ^{48}Ca were also provided for this proposal [50] and are shown in Fig. 9. The effect is qualitatively similar to lead, but slightly smaller due to the smaller neutron excess. The calculation shows a clear enhancement in a_1 over the isoscalar-corrected "naive" case that grows with increasing x. There is essentially no difference at $x = 0.2$, and a 5% difference at $x = 0.7$. We will be able to measure a_1 across this x range with a statistical precision that is typically below 1% and systematic uncertainties of 0.5-0.7%.

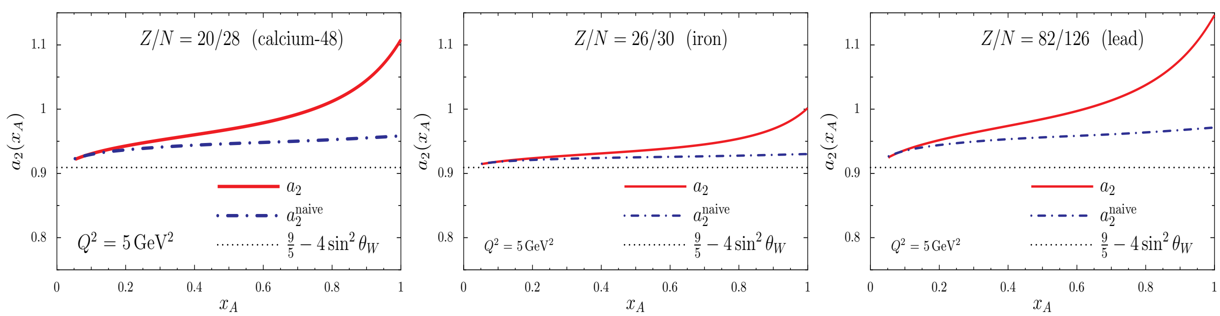

Figure 9: Predictions for a_2 for ^{48}Ca (left), iron (center), and lead(right) from [4, 50]. Note that the curves use a different convention and refer to a_2, which is the same as a_1 in our nomenclature.

4.2.2 Nuclear Parton Distributions

We consider data from PDF fits to understand present constraints in this sector and to consider the precision for new data required to become a significant test. First, we look at the nCTEQ nuclear PDF fits done by Refs. [31] and [32], discussed in Sec. 3.3.3. There the authors varied the contributions of neutrino charged current data with the standard DIS and Drell-Yan data. If there are flavor-dependent variations in the nuclear distributions, the discrepancy between the two in those fits provides an idea on their size.

The results of the a_1 calculations from this fit are shown in Fig. 10. The change in slope of a_1 of about 5% is remarkably consistent with the CBT calculation in the range of $0.2 < x < 0.7$. The fits including any neutrino data have a very different behavior than the neutrino-free fit in terms of the modification. This suggests that there is a lack of constraint on the order of a few percent in the DIS/Drell-Yan data in this observable, which is perhaps not surprising considering the unique flavor sensitivity of neutrino scattering.

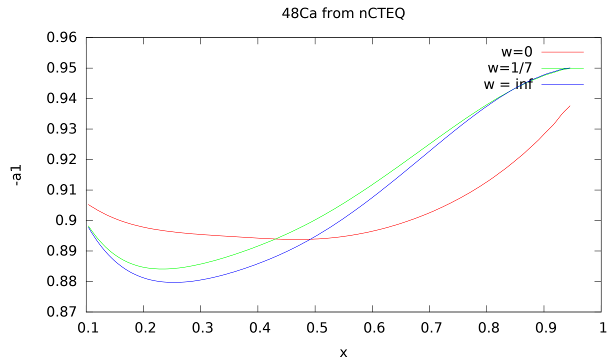

Figure 10: a_1 predictions from the nCTEQ data set assuming various weighting between pure DIS and Drell-Yan ($w = 0$) and pure neutrino data $w = \infty$ from Refs. [31] and [32] for ^{48}Ca. Inclusion of any fraction of neutrino data dramatically shifts the fit demonstrating the weakness of DIS data to this observable. The change in slope is about 5% over our x range and is consistant with the CBT calculation.

4.2.3 Scaling models based on the EMC-SRC correlation

The observed correlation between the EMC effect and the contribution of SRCs has generated much interest and several ideas as to what underlying physics might connect these phenomena [12]. Unfortunately, we do not have calculations that provide quantitative predictions for the EMC effect or its flavor dependence. We can, however, take various ideas that have been proposed to explain the correlation and use this to predict the scaling of the EMC in various nuclei. Older parameterizations assumed that the EMC effect depended on the density, so density distributions for protons and neutrons in various nuclei can be used to make predictions of the relative size of the EMC effect in these nuclei, as well as predicting the flavor dependence based on the difference of the densities observed by protons and neutrons in the nucleus.

More recent proposals include the idea that the local environment of the struck nucleon drives the EMC effect, and so the EMC effect would scale based on the local density for protons and neutrons in the nucleus. It has also be proposed that the EMC effect might be associated with high-virtuality nucleons, which would suggest that the EMC effect might scale with the fraction of the nucleon distribution at very high momenta, the average virtuality of the nucleons, or their average kinetic energy.

The flavor dependence associated with these various these scaling assumptions were evaluated in light nuclei, up to $A = 12$, using the one- and two-body momentum and density distributions from *ab initio* Quantum Monte Carlo Calculations [51]. The predicted A dependence of the EMC effect in light nuclei showed a clear difference between the assumption of scaling with average density and the other pictures [5], shown in Fig. 11 along with linear fits to each of these scaling assumptions. The green points represent the prediction based on assuming that the EMC effect scales with average density seen by the protons and neutrons. While small, this model still yields a non-trivial flavor dependence. The other curves represent scaling models motivated by the observed EMC-SRC correlation.

The predictions based on the idea of scaling with local density or high virtuality all show a significant flavor dependence, with an isospin dependence of 15-30% when evaluated at the neutron excess of 48Ca. The CBT model, expressed in terms of this same isospin dependence, yields a 35% effect, while the idea that the EMC effect is driven by the observed np-dominance of SRCs [7] would yield a 40% excess in the EMC effect for up quarks relative to down quarks. In evaluating the sensitivity of the proposed measurement, we take the CBT model as the default signal of a large EMC effect, but note that it will also be important to differentiate between a large effect and a smaller effect (roughly half the size) to have the ability to evaluate predictions within this range.

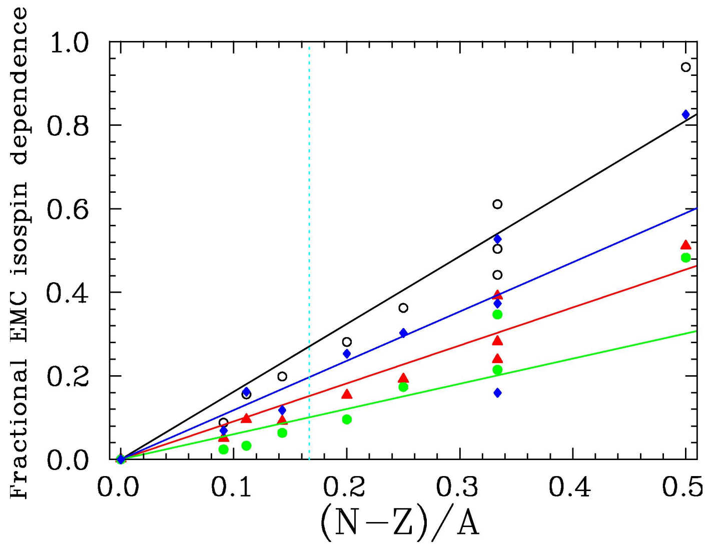

Figure 11: Isospin dependence of the EMC effect vs. fractional neutron excess of the nucleus for the four scaling models. Fraction of momentum distribution above 300 MeV/c (black open circles), average kinetic energy (red triangles), average density (green circles), and probability to be within 1 fm of another nucleon (blue diamonds). The lines are simple unweighted linear fits. The short-dashed line shows the N/Z value corresponding to ^{48}Ca [5].

All of these simple scaling models yield the same qualitative effect, an enhanced EMC effect in minority nucleon, the quantitative prediction is sensitive to the assumed underlying mechanism. As such, a direct measurement of the flavor dependence of the EMC effect is not only needed as input to a wide range of high-energy measurements on non-isoscalar nuclei, it also provides sensitivity to the underlying mechanism. In the simple analysis shown here, we use a linear extrapolation in the fractional neutron excess to make predictions for ^{48}Ca. While we do not have complete and reliable versions of the one- and two-body distributions used in this analysis for ^{48}Ca, significant progress is being made in calculating nuclear structure in this mass range, allowing for a more direct connection with the data. More importantly, a first direct and precise measurement of the flavor dependence will motivate calculations that explicitly attempt to account for flavor or isospin dependence.

4.3 Sensitivity of the Proposed PVEMC Measurement

An evaluation of the statistical and systematic uncertainties for the PVEMC measurement are presented in Sec. 6. Figure 12 shows the projected uncertainties, along with predictions for no flavor dependence and the CBT flavor-dependent result.

To determine the sensitivity of the measurement, we compare the null hypothesis (a_1^{naive}) to projected data generated according to the CBT model. Neglecting the normalization uncertainty, this yields $\chi^2 = 99.8$ for 9 degrees of freedom. Even shifting the data down by twice the normalization uncertainty, the comparison yields $\chi^2 = 61$ corresponding to a 6.2σ measurement.

For comparisons to the sensitivity EMC effect ratios, evaluated in the next section, we also look at the sensitivities when we analyze the signal in terms of the x dependence. For this, we take a linear fit to the data and compare the slope the fit to that of the null hypothesis curve. For the cross section ratios, this is a useful approach as it is insensitive to the larger normalization uncertainty for those measurements. Examining the slope, the projected data yield a 3.7σ deviation from the null hypothesis (Δslope$= 0.086 \pm 0.024$). Because

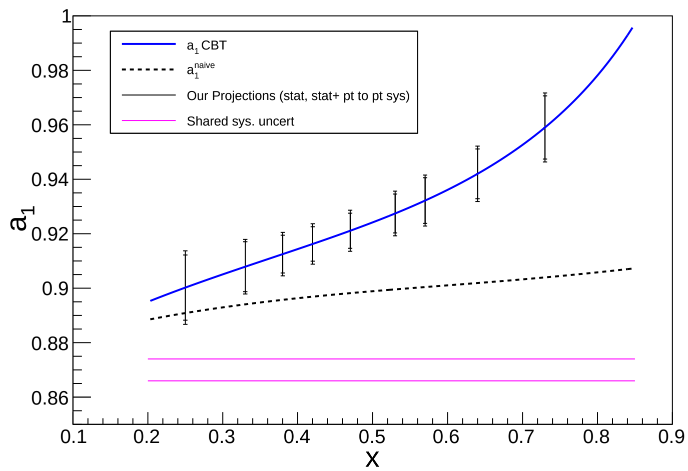

Figure 12: Projected measurement values (black points) compared to expectations with and without a flavor-dependent EMC effect. The black dotted line is the expectation with no flavor dependence, the blue curve is the CBT calculation, and the magenta band indicates the $\pm 1\sigma$ normalization uncertainty on the measurement.

of the small normalization uncertainty, it is more sensitive to look at a_1 at large x values, where the linear fit yields a 5.5σ deviation from a_1^{naive} ($\Delta a_1 = 0.027 \pm 0.005$).

The CBT model yields a relatively large flavor dependence compared to other estimates provided in Sec. 4.2.3, with an isospin asymmetry of 0.35, with other estimates ranging from 0.15-0.40. Thus, the 6.2σ sensitivity to the CBT calculation also corresponds to a $> 3\sigma$ sensitivity all but the smallest of these estimates, and a 4.4σ difference between the largest and smallest predictions in this range. Thus, it has both discovery potential for flavor dependence, but also the precision to differentiate between models that predict larger or smaller signals.

4.4 Relation to Other Experiments

4.4.1 JLab E12-10-008

Measurements of the EMC effect for ^{40}Ca and ^{48}Ca (and several other targets) will be taken in JLab experiment E12-10-008 [3], and the ratio of ^{48}Ca to ^{40}Ca has some sensitivity to the flavor-dependence of the EMC effect. Figure 13 shows projected results for the ^{48}Ca/^{40}Ca cross section ratio in the region of the EMC effect, where the ^{48}Ca result has had isoscalar corrections applied, as with other EMC effect measurements. The dotted line is the predicted impact of the A-dependence from the SLAC global fit [23], and the blue line shows the prediction of the CBT model.

We quantify the significance of the measurement by taking projected data (assuming CBT flavor dependence) and fitting the slope of the ratio in the EMC effect region, $0.3 \leq x \leq 0.7$. For the projected data, we assume the CBT flavor dependence and take 0.7% point-to-point systematic uncertainties and 0.95% statistical uncertainties, and a 1.4% normalization uncertainty on the ratio. The difference between the slope obtained from the projected data and the slope of the SLAC global fit is Δslope=0.047 ± 0.024 - 2 standard deviations from no flavor dependence. Instead of the slope, we can focus on the large-x data by examining the value of the linear fit at $x = 0.7$. In this case, the deviation from the null hypothesis is (3.1±0.4±1.4)%,

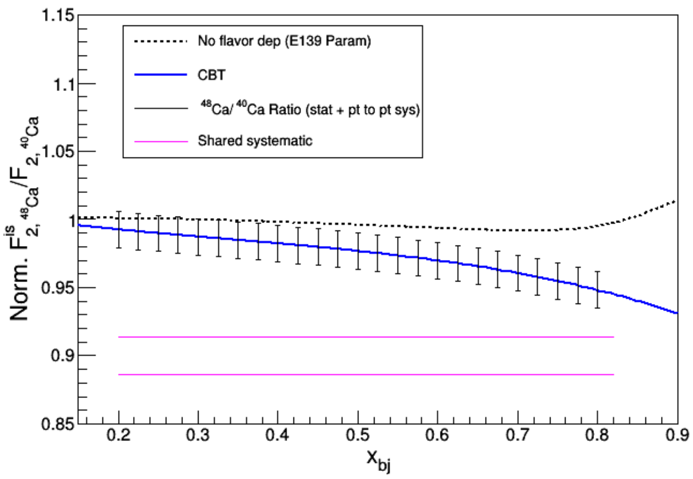

Figure 13: Projected uncertainties for the E12-10-008 ^{48}Ca/^{40}Ca cross section (per nucleon) ratio. Black dashed line is the SLAC E139 global fit, assuming no flavor dependence, the blue curve is the CBT projection, and the magenta band indicates the $\pm 1\sigma$ normalization uncertainty

a 2.1σ deviation. Note that both this and the slope are sensitive to the increase in the large-x data, so these sensitivity tests are not independent.

For the PVDIS measurement, the best sensitivity comes from comparing the projected data, generated according to the CBT model, to the null hypothesis in the DIS regime ($0.3 < x < 0.7$). However, it is clear from Fig. 13 that a modest normalization adjustment will remove most of the sensitivity (as illustrated by shifting the projected data in Fig. 1). For example, if we take projected data according to the CBT model and allow for an overall normalization shift, it only takes a 1.1% shift (0.8% of the projected normalization uncertainty) for the data to be in better agreement with the SLAC curve than the CBT model. For the EMC measurements, the sensitivity for this approach is actually less than that obtained by examining the slope by itself or using just the high-x data. This is because a normalization shift can put the CBT data in good agreement with the SLAC prediction, and simply measuring the total χ^2 doesn't take advantage of the fact that such a shift would yield data systematically above the SLAC curve at low x and below at large x.

A direct comparison between the two is given in Table 1. The small signal of flavor dependence in the ^{48}Ca/^{40}Ca ratio, combined with the 1.4% normalization uncertainty, significantly limit the sensitivity of such comparisons. Such measurements will yield only $\sim 2\sigma$ differentiation between the CBT model and no flavor dependence, and not have the ability to provide any meaningful differentiation between large or small flavor dependence signals. As such, the PVEMC data will be critically important no matter what is observed in the ^{48}Ca/^{40}Ca ratios.

Finally, note that in addition to the fit uncertainties, there are small model-dependent uncertainties associated with the model used to extrapolate from A=40 to A=48 and our knowledge of the ratio of neutron-to-proton structure functions, needed to provide the isoscalar result for A=48.

While E12-10-008 will measure other nuclei, the calcium comparison is the most sensitive test. For heavy nuclei such as Au and Pb, the size of the EMC effect is somewhat larger, as is the fraction neutron excess, but there is no isoscalar 'baseline' available for comparison. Lighter nuclei show a smaller EMC effect and generally have smaller neutron excesses, yielding smaller sensitivity to flavor dependence. They have the the additional complication that the A dependence in light nuclei is less well understood, as contributions related to clustering and/or short-range correlations are strongly A dependent in light nuclei. As such, a similar measurement comparing ^{10}B to ^{9}Be or ^{11}B would have a large model-dependent uncertainty. As noted above, parity-violating scattering is insensitive to the EMC effect, as long as it is identical for up and down quarks, so even a nucleus like ^{9}Be, which has significant cluster structure, can be used to examine the flavor dependence without worry about the detailed structure of the nucleus.

4.4.2 JLab E12-08-103 - MARATHON

A comparison of the EMC effect in ^{3}H and ^{3}He would be sensitive to the flavor dependence of the EMC effect, but this comparison is much more sensitive to the neutron structure function. While the MARATHON experiment has measured the ^{3}H/^{3}He cross section ratio in the EMC region, it uses estimated upper limits on the difference of nuclear effects in ^{3}H and ^{3}He to provide an improved extraction of F_{2n}/F_{2p} [42].

Questions have been raised [45, 46] about the model used for the nuclear effects in Ref. [42], as different models of the nuclear effects have some impact on the extraction of F_{2n}/F_{2p}. In particular, allowing for large, flavor-dependent modification significantly increases the uncertainty in the extraction of the neutron structure. For example, Taking the pdfs for ^{3}H and ^{3}He based on the extrapolation from np-SRC dominance [7] (as used in the SIDIS analysis 3.3.4), the impact of the flavor dependence is $\sim$2% at x=0.75, roughly twice the size of the correction assumed in extracting F_{2n}/F_{2p} [52]. Note that this 1% change in the high-x ratio is significantly larger than the 0.2% uncertainty assumed in the nuclear effects for the extraction of F_{2n}/F_{2p}, making this an important potential issue in the neutron extraction. Ref. [46] performs a global analysis and, effectively, uses the inconsistency between F_{2n}/F_{2p} as extracted from D/p and ^{3}H/^{3}He to constrain the nuclear effects, including their flavor dependence. However, several assumptions have to be made to allow for this extraction and, as with the global pdf analyses mentioned in Sec. 3.3.3, the extraction of flavor-dependent effects from the tension in different data sets is extremely sensitive to the details of the uncertainties as determined by the experiment and their treatment in the analysis.

Other experiments can also provide model-independent extractions of the neutron structure function, but this will not allow a comparison of the nuclear effects unless the precision is significantly better than the extraction from MARATHON. More specifically, the total uncertainty in the neutron extraction must be smaller than the model-dependent contribution to MARATHON's extraction before limits can be set beyond the assumed upper limits taken in MARATHON's extraction of F_{2n}/F_{2p}. As noted above, the difference between the model of the nuclear effects used in the MARATHON experiment and in the flavor-dependent EMC effect based on np-dominance is $\sim$1% at large x, while the experimental uncertainties in this region are $\sim$1.5%, meaning that even with perfect knowledge of the neutron structure, MARATHON will have no meaningful sensitivity to the flavor dependence. This is not too surprising, as while the difference in N/Z for the nuclei is large, the total EMC effect is very small for A=3 nuclei.

4.4.3 JLab PR12-09-004, LOI12-19-005 - SIDIS

Proposal PR12-09-004 [37], "Precise Measurement of π^+/π^- Ratios in Semi-inclusive Deep Inelastic Scattering Part II: Unraveling the Flavor Dependence of the EMC Effect", aimed to use a comparison of π^+ and π^- production from Au to look for flavor dependence in the EMC effect. The proposal was deferred, in large part due to questions about how well the data could be interpreted in terms of flavor dependence, given the possibility for differences in hadron attenuation effects for π^+ and π^- as well as questions regarding possible differences in the p_T dependence of the pion yields since the proposed measurement would only detect pions emitted along the virtual photon 3-momentum. The degree to which factorization in the SIDIS reaction would be satisfied was also a concern.

LOI12-19-005 [38], "Next Generation Tritium Experiments in CLAS12", raised the idea of comparing π^+ and π^- production from ^{3}H and ^{3}He as a way to minimize the uncertainties associated with nuclear effects. As noted in Sec. 3.3.4, there were indications of observable signals for extreme cases, in particular for the calculation where the EMC effect is carried entirely by d quarks. More realistic models predict significantly smaller effects, as discussed in Sec. 3.3.4.

5 Experimental Design

We choose a $2.4\ \mathrm{g/cm^2}$ ^{48}Ca target ($x/X_0 = 12\%$) at $80\ \mu$A with maximum longitudinal beam polarization as the general production conditions. *The experimental layout we propose is identical to the existing SoLID PVDIS proposal [47], with the replacement of the LD_2 target ladder with our ^{48}Ca target ladder.* For 66 days of production, a 0.7-1.3% statistical uncertainty for $0.2 < x < 0.7$ can be obtained (Fig. 14). A ∼0.5-0.7% systematic uncertainty per-bin is anticipated, discussed in Sec. 6.2. Our sensitivity to the CBT model is shown in Fig. 12 and is ∼6σ including all shared systematics.

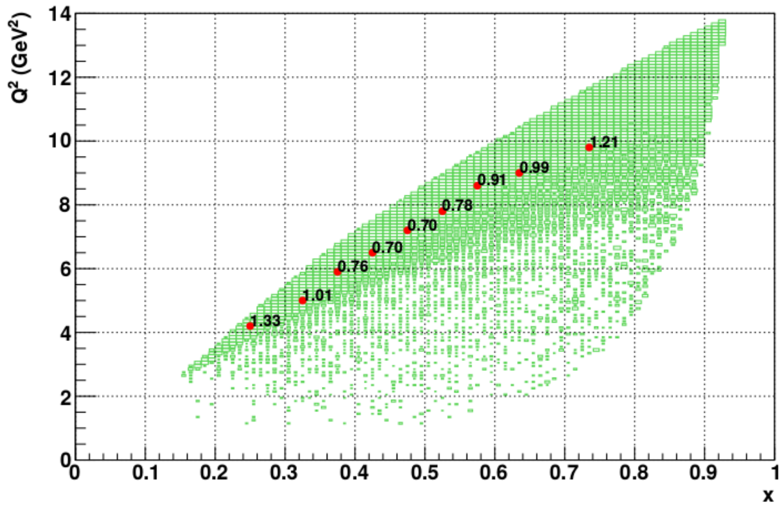

Figure 14: Our statistical precision for A_{PV} for x and Q^2 bins in %.

This is a true "counting mode" parity-violating experiment in contrast to parity-violating experiments in the past that have used integrating detectors gated over the beam-helicity window. The full SoLID program is still under a detailed design and review process, which is more fully described in the SoLID pre-CDR document [53]. Here we cover the relevant aspects of the design and the anticipated performance.

Most aspects of this experiment are less demanding than the approved PVDIS LD_2 experiment for the following reasons:

- this proposal utilizes a solid target with good thermal properties and is not subject to effects such as boiling,
- less total target material mass, generally providing lower rates,
- the physically short target has better controlled acceptance and collimation.

This target has a 12% radiation length, which is a factor of two larger than the LD_2 target, and presents a few challenges. First, the overall radiative corrections due to external bremsstrahlung is approximately doubled. Direct photons from the target are increased as well as the pion photoproduction rates. Combined with the fact the target has a neutron excess, the relative number of π^- to DIS events is increased.

A suite of simulations has been developed in the Geant4 framework which includes a complete and detailed representation of the target and detector geometries, Fig. 15, and includes particle showering and optical photon production. In addition, event generators for deep inelastic scattering based on the CTEQ6M

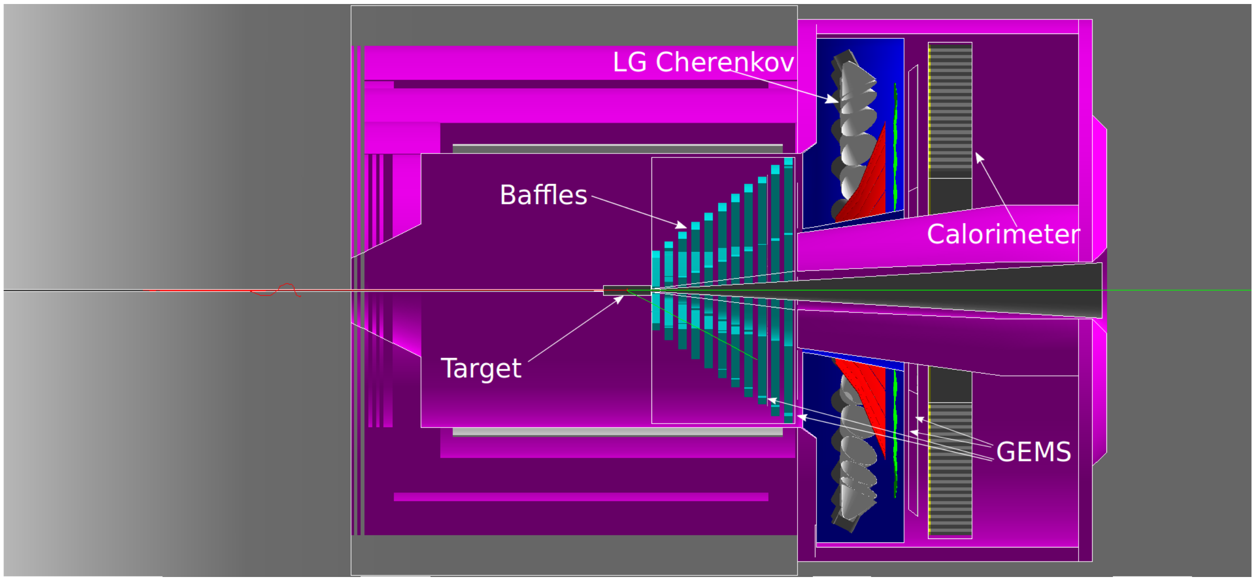

Figure 15: SoLID side-view of the Geant4 configuration with full detector setup.

PDFs [54] and pion production based on a SLAC photoproduction data parameterization [55] with the equivalent photon approximation for the electroproduction data have been developed. We utilize this simulation to generate the following rate and response estimates.

5.1 Targets

We propose to use a 2.4 g/cm^2 ^{48}Ca target, assumed to be 95% isotopically pure. A 0.8 g/cm^2, 90% pure target was employed by the $x > 2$ experiment [56] at 50 μA, Fig. 16, and the parity violating experiment, CREX [57] with beam current of 150 μA at 2.2 GeV used 2.4 g/cm^2 95.99% pure ^{48}Ca target with 3.84% ^{40}Ca impurities. The target design used in previous experiments will need to be modified to allow for full acceptance of all scattering angles when the raster is employed.

Calcium has relatively robust thermal properties which are advantageous for this experiment: a melting point of 840° C and a high thermal conductivity of 200 W/m/K. While the melting point is an absolute upper limit, calcium undergoes crystalline structure changes at lower temperatures. A 4×4 mm^2 raster will be used to distribute the heat load. This experimental configuration will have a power deposited from the beam of about 600 W, but thermal calculations showed that with sufficient cooling on the support frame held at room temperature, operate at only 100° C, within heating limits and below the CREX ΔT.

The original design was a disk with a diameter of at least one inch so that detected electrons would not pass through the target holder (left panel, Fig. 17). Since the previous submission, we have modified the target design to significantly reduce the amount of ^{48}Ca needed, while maintaining the same thickness and reducing multiple scattering. Rather than a disk with a uniform radius, the radius will reduce along the length of the target, significantly reducing the amount of target material. The holder of the target, made of beryllium or aluminum, will have to be thick enough to allow sufficient heat conduction out of the target, but the added thickness will be significantly less than the amount of calcium removed, reducing both multiple scattering and radiation for the outgoing electron. We estimate that this design will allow us to reduce the amount of ^{48}Ca used by 30% or more, with no negative impact on the physics measurement. A detailed analysis of the heat transfer through the target holder will be required to finalize the design, but the target group does not believe that there will be issues obtaining sufficient mechanical support or heat conduction [58].

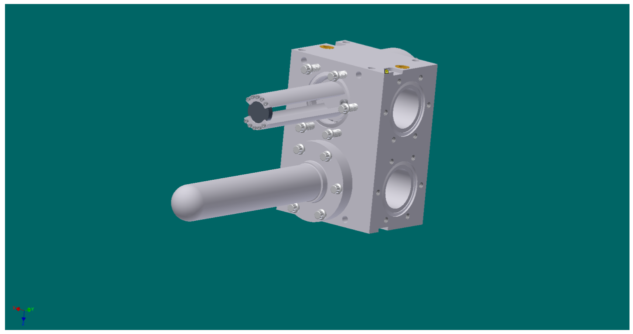

Figure 16: A CAD design of the existing ^{48}Ca target for E08-014. Two identical ^{40}Ca and ^{48}Ca targets were mounted in the ladder design.

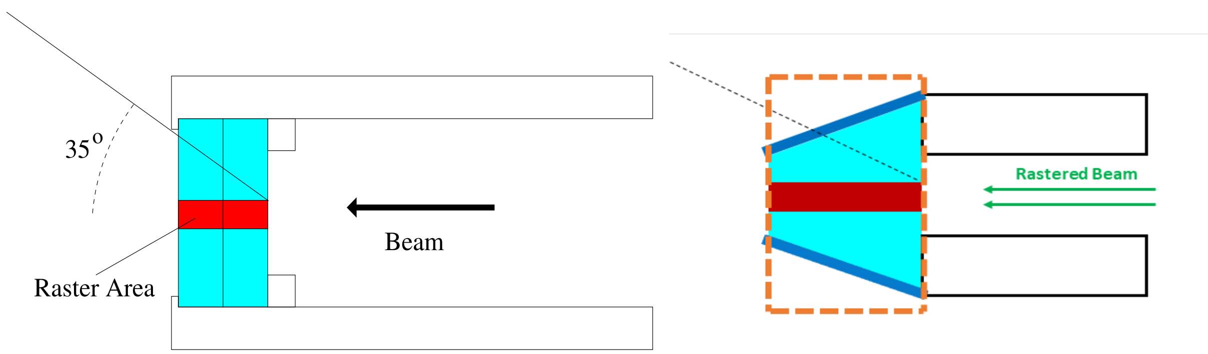

Figure 17: Schematic drawings of the old (left) and new (right) target design concepts. In the old design, the target was a disk of a least 1 inch diameter. In the new design, the calcium is pressed into a conic section made of beryllium (or aluminum). The orange box in the new design indicates the size of the ^{48}Ca disk in the original design. While the outgoing electrons now go through the target holder (estimated to be 1.5-3mm to allow for sufficient heat conduction), this will yield less multiple scattering and radiation length due to the reduced amount of calcium.

Auxiliary targets will be required in the same ladder to provide calibrations and tests, described in Sec 5.4. In particular, a set of several carbon foils spaced ±20 cm (with one specifically at the center position of the ^{48}Ca target). Aluminum targets with known radiation thicknesses of 1%, 5%, and 10% will help provide validation of unfolding external radiative effects and a LH_2 target will be used for momentum calibration.

5.2 SoLID

The SoLID project is a large acceptance, high luminosity spectrometer and detector system designed for experiments that require a broad kinematic acceptance at high rates. It presently has five approved experiments covering physics topics such as PVDIS on LD_2 and LH_2, semi-inclusive DIS on polarized targets, and J/ψ production at threshold. We will focus on the PVDIS configuration, which consists of

- A 3 m diameter solenoidal magnet that provides a central field of ~ 1.5T and field integral of about 1.8 T · m.
- A set of collimators ("baffles") which block low momentum particles and line-of-sight photons.

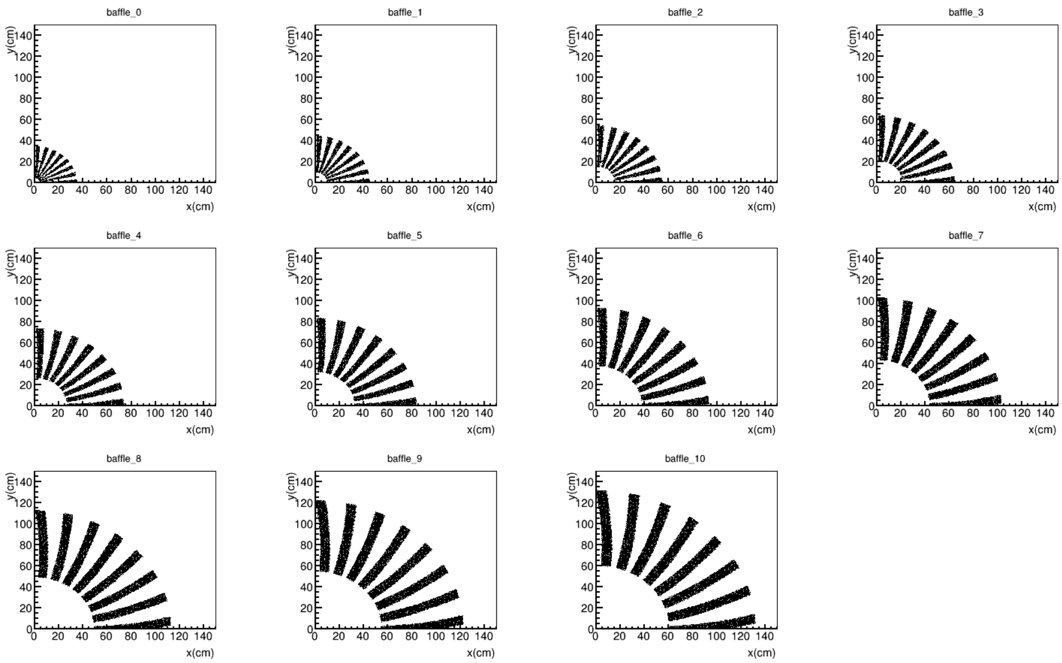

Figure 18: Projection of the baffle lead “spokes” to block low momentum particles.

- A set of five GEM layers which provide high resolution, hit-based tracking in a high luminosity environment.
- A light gas Cherenkov detector for pion identification.
- An electromagnetic calorimeter in a shower-preshower configuration which also provides some pion rejection capabilities and acts as the primary trigger and an additional point in tracking.

This configuration with baffles nominally has $2\ \mathrm{rad}$ azimuthal acceptance, polar angle acceptance of 22-35°, and momentum acceptance of $1 - 7$ GeV. Azimuthally it is divided into 30 predominantly independent sectors which can operate at a total of ~ 600 kHz in inclusive running. A representation of this setup from our Geant4 simulation is shown in Fig. 15.

5.2.1 Baffles

The baffles provide a reduction in the large low-momentum flux and block line-of-sight photons from the downstream detectors. They consist of 11 lead “wheels” which divide the acceptance into 30 sectors, Fig. 18. The curvature of the arms are designed in such a way that particles within a specific momentum window will pass in between the arms to the detectors.

The coverage of the baffles defines the azimuthal and momentum acceptance for the spectrometer. Nominally, the first baffle reduces the flux by a factor of two and particles less than 1 GeV are blocked by successive baffles, leading to an overall charged rate reduction of about an order of magnitude. The momentum acceptance for the accepted particles follows from several geometric and design effects and is shown for the ^{48}Ca configuration in Fig. 19.

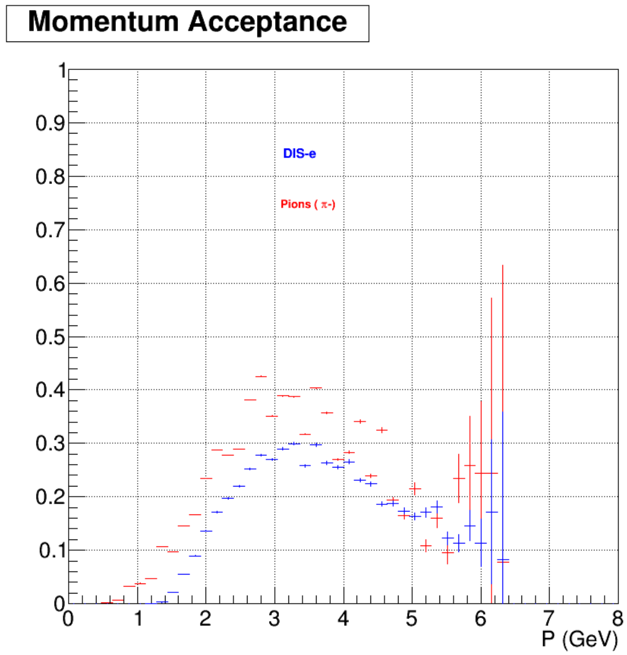

Figure 19: Electron and π^- acceptances from the baffles. Differences between these are due to varying angular distributions and the fact that π^- have longer interaction lengths.

5.2.2 GEMs

The GEM (gas electron multiplier) trackers originally developed at CERN provide high resolution tracking in high rate environments. They have been demonstrated to work at rates up to 100 MHz/cm^2 and provide a hit resolution up to 70 μm with a 200 μm readout pitch. We employ five planes of GEM chambers, three interleaved with the rear baffle planes and two after the light-gas Cherenkov detector, detailed in Table 2. Each plane consists of 30 individual GEM modules and are aligned such that the gaps of the first three chambers lie over a baffle spoke, Fig. 20. The pitch will be 0.4 mm for the first three GEMs and 0.6 mm in the rear GEMs as the rates are lower.

Significant contributions to the GEM rates come from not only DIS electrons, but also π^- and photons. For the latter, the response is highly dependent on the photon momentum and the radiation thickness of the detector. Figure 21 shows the results from Geant4 simulation for the photon response with a 0.5% radiation

Location	Z (cm)	R_{min} (cm)	R_{max} (cm)	Surface (m^2)	# chan
1	157.5	51	118	3.6	24 k
2	185.5	62	136	4.6	30 k
3	190	65	140	4.8	36 k
4	306	111	221	11.5	35 k
5	315	115	228	12.2	38 k
Total				$\approx$ 36.6	$\approx$ 164 k

Table 2: GEM design parameters for the SoLID PVDIS configuration.

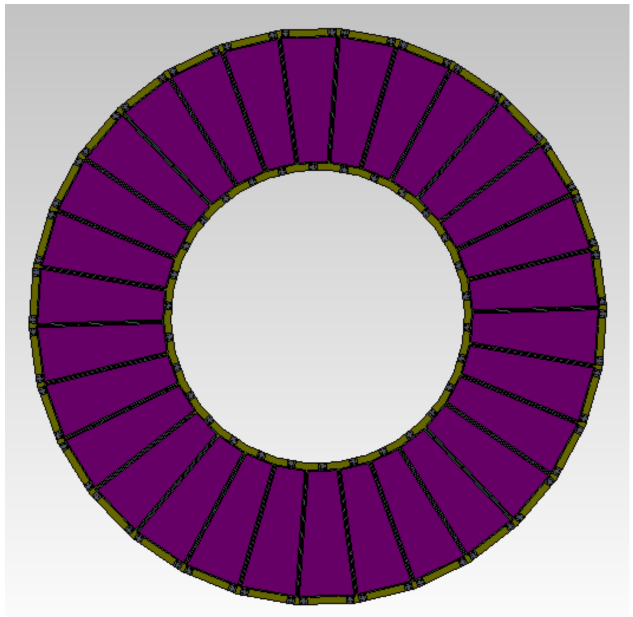

Figure 20: CAD drawing of a GEM plane for the PVDIS configuration.

length GEM, which drops for photons < 1 MeV. A comparison between hit rates for our proposal and simulations for the LD_2 measurement are shown in Table 3.

The radial GEM rates are presented in Fig. 22. The particle rates at the last GEM, which will be incident on the EM calorimeter, are broken down by particle type and shown in the Table 4. The initial π^+ background is heavily suppressed by the combination of baffle design and the solenoidal magnetic field but will also be produced in interactions within the baffle material. A combination of triggering and off-line analysis is required to suppress the π^- background to desired level. The DIS electron rates at the last GEM for various x-cuts is shown in the Table 5.

The background rates are much greater than the DIS rates at the entrance to the EM calorimeter. The

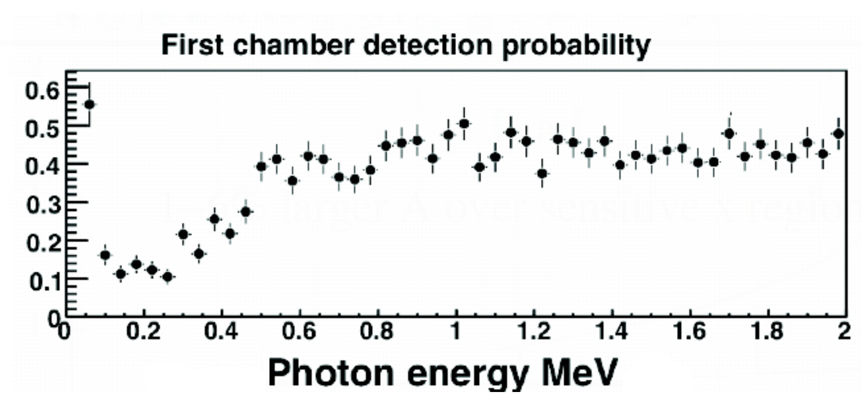

Figure 21: Geant4 calculation results for photon interaction probabilities with GEM chambers from Ref. [59].

GEM plane	LD_2 background ($kHz/mm^2/\mu A$)	^{48}Ca EM background ($kHz/mm^2/\mu A$)	^{48}Ca EM background (no baffles) ($kHz/mm^2/\mu A$)
1	6.8	4.8	49.4
2	3.0	2.1	32.3
3	1.1	0.8	9.9
4	0.7	0.5	6.4

Table 3: The low energy EM background radiation at GEM detectors compared for ^{48}Ca and LD_2 targets with and without baffles.

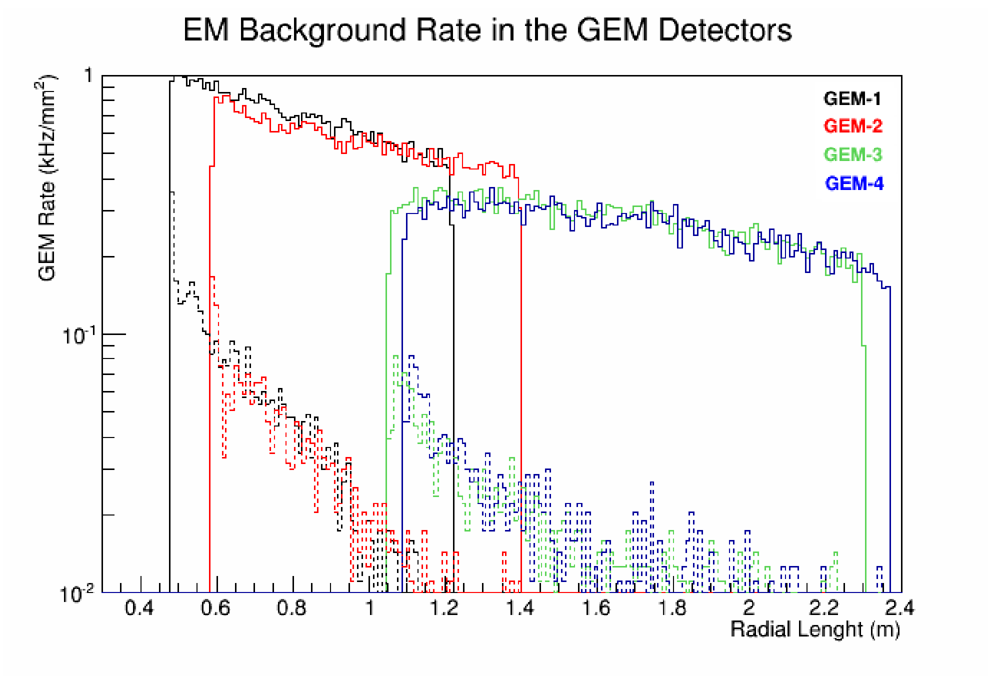

Figure 22: The design of the baffle structure minimizes the EM background rates at the GEM detectors. The solid lines shows background rates with no baffles and the dashed lines show the rates with the baffles. The baffle structure reduce the background rates by almost a factor of 10.

Momentum range (GeV)	π^- (MHz)	π^+ (MHz)	$\pi^0(\gamma)$ (MHz)	Proton (MHz)	EM (γ, e$\pm$) (GHz)
p $>$ 0.0 GeV	618	283	70123	483	844
p $>$ 0.3 GeV	439	153	438	417	n/a
p $>$ 1.0 GeV	123	18	37	51	0.0
p $>$ 3.0 GeV	2	0.01	0.04	0.004	0.0

Table 4: Breakdown of rates based on the particle types for ^{48}Ca target at 80 μA.

Momentum range (GeV)	^{48}Ca (kHz)
DIS Total	228
W $>$ 2.0 GeV, $\mathrm{x_{Bjk}} > 0.20$	207
W $>$ 2.0 GeV, $x_{Bjk} > 0.55$	15
W $>$ 2.0 GeV, $x_{Bjk} > 0.65$	3

Table 5: Breakdown of DIS rates for ^{48}Ca target at 80 μA.

rates below $\mathrm{p} < 1.0$ GeV are predominantly electromagnetic backgrounds. The high energy $\mathrm{p} > 1.0$ GeV backgrounds are dominated by contributions from pions and protons.

5.2.3 Calorimeter

The electromagnetic calorimeter serves as the primary trigger as well as an independent means for rejecting π^- backgrounds. It it configured in a hexagonal preshower-shower configuration and consists of "shashlyk"-style blocks with 50 cm of interleaved sampling lead and scintillator plates with a fiber readout, Fig. 23, with a radial coverage of 110-265 cm or $\sim$18 m^2. Each module has a lateral coverage of about 100 cm^2 providing adequate position resolution, background sensitivity, and cost for a total of about 1800 modules. The shower and preshower are read out through 100 1-mm-diameter waveshifting fibers that are threaded down the module and run to the rear of the solenoid. They are coupled to clear fibers and then to multianode PMTs (1 PMT per module).

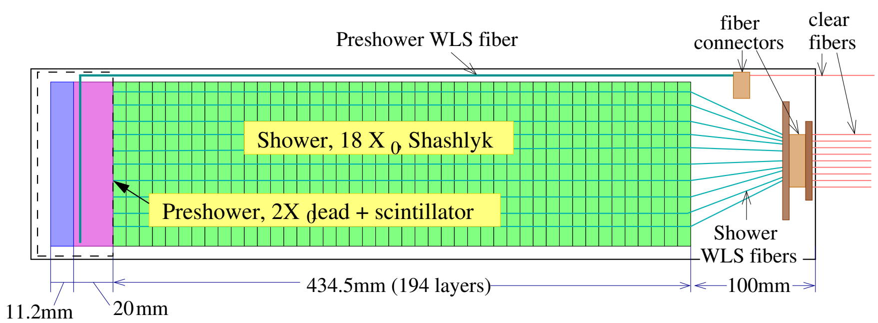

Figure 23: Cross section of an electromagnetic calorimeter module and absorber sheets.

The momentum resolution requirements for the shower are relatively modest, as it must primarily provide a trigger above the low energy background flux, and reconstruct a reasonably good position and energy. For our modules, a $4\%/\sqrt{E}$ resolution has been simulated. A good position resolution is important as in the high luminosity environment, the reconstructed point will serve as a base for track reconstruction. Accounting for the energy distributions of tracks that are not normal to the face of the detector leads to a RMS of $<$1 cm is achieved in the radial and azimuthal directions.

As a method of pion rejection (in combination with the gas Cherenkov), the preshower and shower energy deposition information can be used. For our configuration, at a 100:1 rejection factor is anticipated (improving with particle momentum) for $E > 2$ GeV, Fig. 24 while maintaining a 95% electron efficiency.

Our simulations to determine the performance of the EM calorimeter are based on DIS events with realistic backgrounds incident on the EM calorimeter. These simulations provide trigger efficiencies for DIS electrons and all the background types. The trigger efficiencies and rates on particles incident on the

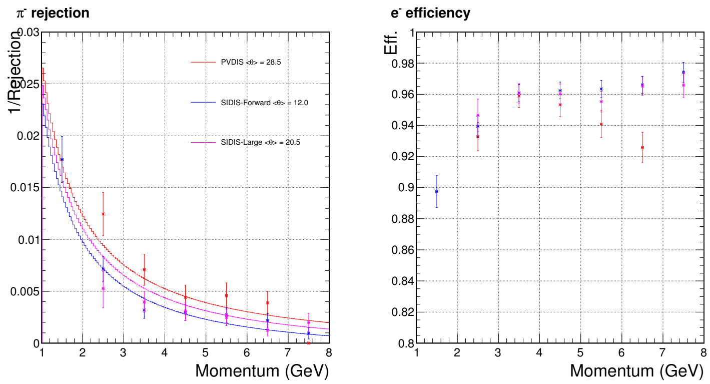

Figure 24: π^- rejection and electron efficiency for calorimeter. Red points and curves are for calorimeter in PVDIS configurations

full coverage of the EM calorimeter are used to extract the total trigger rate for the EM calorimeter. In order to further optimize the calorimeter performance, each 12° azimuthal sector in the calorimeter is divided into two 6° segments based on the background rate which varies due to the baffle structure. The low (high) rate section is shown in the top (bottom) panels of Fig. 25.

It is observed by dedicated EM calorimeter simulations that the pile-up effects are not significant for particles with momentum $\mathrm{p} > 1\ \ \mathrm{GeV}$ but is an important effect for particles with $\mathrm{p} < 1\ \ \mathrm{GeV}$. Due to this effect, the trigger rates for the lowest energy particles cannot be broken down to particle type in a straight forward manner and we quote only a total trigger rate. Table 6 summarizes this for ^{48}Ca target.

The luminosity for this experiment is $\sim 2 \times 10^{37}$ Hz/cm^2 (calculated per nucleus) or a factor of 3 smaller per-nucleon than the LD_2 measurement. The additional radiation dose is about 36 kRad compared to the design specification of 400 kRad and present program of less than 200 kRad of running.

5.2.4 Light Gas Cherenkov

The light gas Cherenkov detector provides rejection of π^- background, which is difficult to otherwise suppress from the e^- DIS signal. In the PVDIS configuration, it is proposed to consist of a ~ 1 m gas radiator of 65% C_4F_8O and 35% N_2 (refractive index 1.001 or $\pi^\pm$ threshold of 3.2 GeV) and is divided up into 30 sectors matched to the baffle segregation. For each sector there are two spherical mirror sections to provide light collection over a broad radial range which focus into a Winston cone/PMT set (see Figure 26). The PMTs are 8×8 pixel multi-anode bialkali PMTs arranged in a 3×3 array and are shielded from the residual field with a mu-metal cone. To help reject pion triggers, the Cherenkov is placed in coincidence with the calorimeter through a sum of all 9 PMTs.

The photoelectron distributions generated as a function of angle for DIS electrons is shown in Fig. 27. A threshold was chosen dependent on the momentum where the pion rejection efficiency was maximized while losing minimum number of electrons and is shown in Fig. 28. The rejection factor for 2-3 GeV pions is 1000:1 - 400:1, worse for the higher energy π. In combination with the 100:1 independent rejection factor from the preshower/shower providing an overall rejection of 10^5 - 4×10^4 up to 3 GeV and at least 100:1 above that. The total rates seen by the Cherenkov and the estimated trigger rates are summarized in the Table 7. The π^-/e^- ratio we anticipate as a function of momentum is shown in Fig. 29 for both the LD_2 measurement and ^{48}Ca.

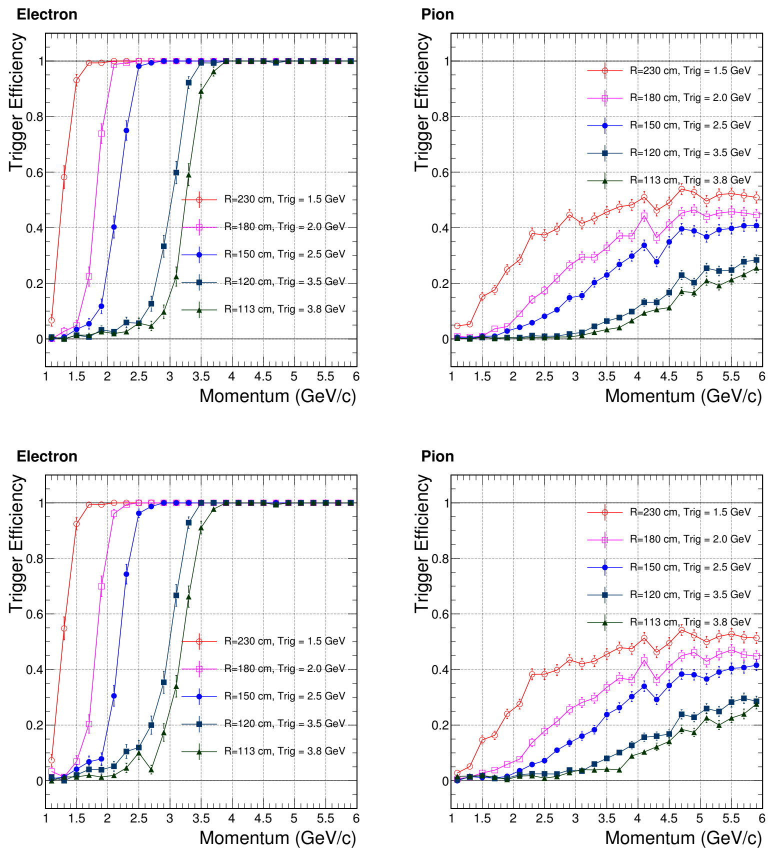

Figure 25: Electromagnetic calorimeter trigger performance for the low rate azimuthal region for e^- (left) and π^- (right). Top figures are for the low rate section; bottom for the high rate.

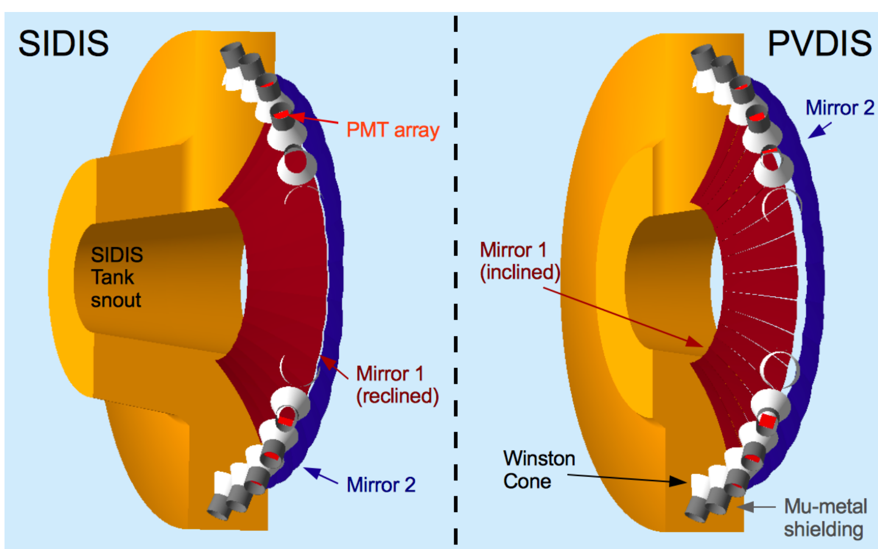

Figure 26: Geant4 cross section of the light gas Cherenkov detector for the SIDIS (left) and PVDIS (right) configurations.

region	full	high	low
rate entering the EC (kHz)			
e^-	240	129	111
π^-	5.9×10^5	3.0×10^5	3.0×10^5
π^+	2.7×10^5	1.5×10^5	1.2×10^5
$\gamma(\pi^0)$	7.0×10^7	3.5×10^7	3.5×10^7
p^+	4.8×10^5	2.1×10^5	2.7×10^5
sum	7.1×10^7	3.6×10^7	3.6×10^7
Rate for $p < 1$ GeV (kHz)			
sum	8.4×10^8	4.2×10^8	4.2×10^7
trigger rate for $p > 1$ GeV (kHz)			
e^-	152	82	70
π^-	4.0×10^3	2.2×10^3	1.8×10^3
π^+	0.2×10^3	0.1×10^3	0.1×10^3
$\gamma(\pi^0)$	3	3	0
p	1.6×10^3	0.9×10^3	0.7×10^3
sum	5.9×10^3	3.3×10^3	2.6×10^3
trigger rate for $p < 1$ GeV (kHz)			
sum	2.8×10^3	1.4×10^3	1.4×10^3
Total trigger rate (kHz)			
total	8.7×10^3	4.7×10^3	4.0×10^3

Table 6: Calorimeter trigger rates based on ^{48}Ca target. DIS and background rates that enter full coverage of the EC are considered for the resulting trigger rates. Trigger is broken down to $p < 1$ GeV and $p > 1$ GeV particles and for the "low" and the "high" background regions. The total rate for the sum of 30 sectors are shown here. The simulated pion rejection and electron efficiency values are shown in Fig. 25.

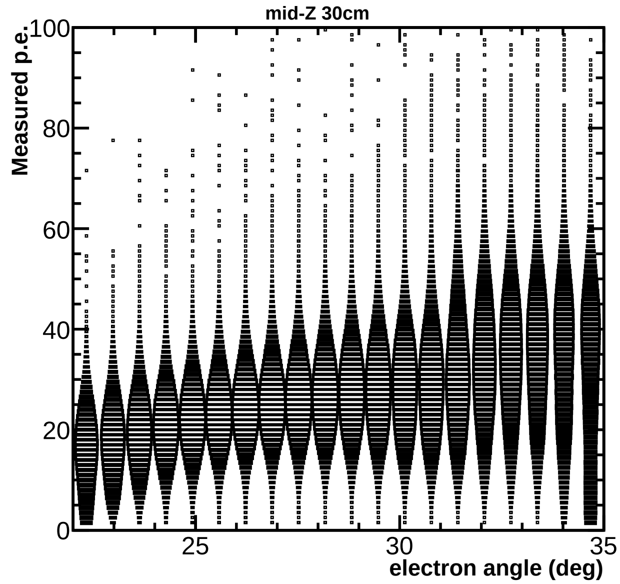

Figure 27: Simulation results for collected photoelectrons for the PVDIS LD_2 experiment for the middle of the target.

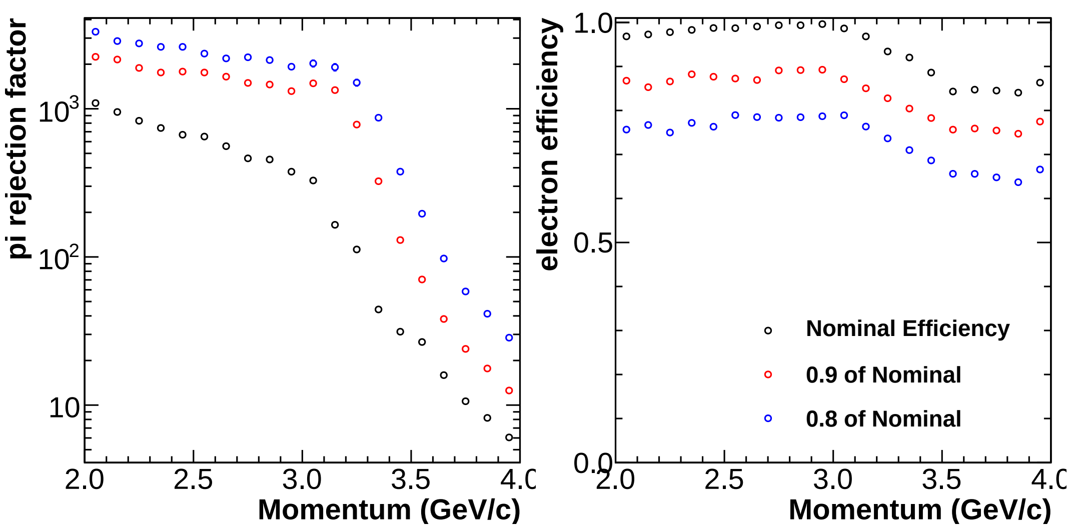

Figure 28: Simulation results for the pion rejection factor and electron detection efficiency for a “nominal” case where π^- rejection is maximized and and minimizing the loss of electrons as well as the $\sim 10\%$ and $\sim 20\%$ e^- loss cases.

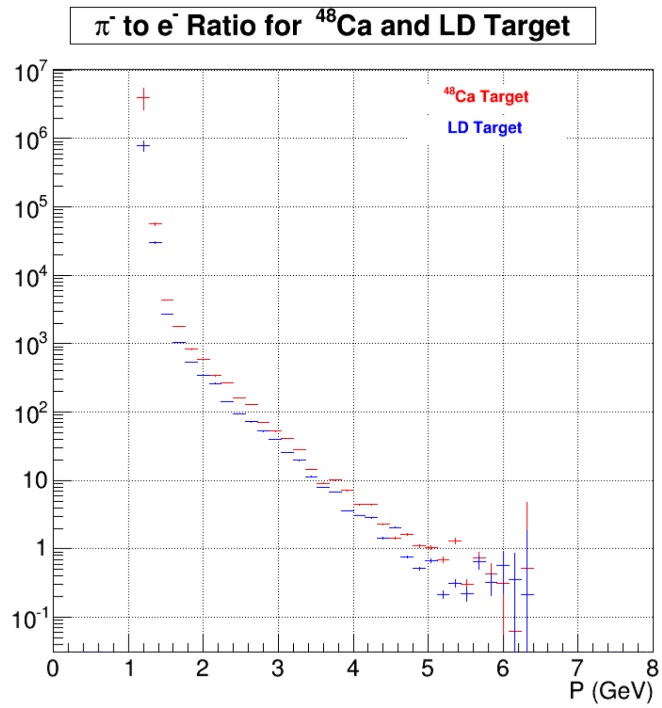

Figure 29: A comparison of π^- to e^- for LD_2 and ^{48}Ca targets. The ratio for ^{48}Ca is about 50% larger.

	Total Rate for p $>$ 0.0 GeV (kHz)	Rate for p $>$ 3.0 GeV (kHz)
DIS	240	73
π^-	5.9×10^5	1.6×10^3
π^+	2.7×10^5	40
$\gamma(\pi^0)$	7.0×10^7	40
p	4.8×10^5	4
Sum	7.1×10^7	1.7×10^3
Trigger Rate from Cherenkov (kHz)		
	Trigger Rate for p $>$ 1.0 GeV (kHz)	Trigger Rate for p $>$ 3.0 GeV (kHz)
DIS	223	66
π^-	193	49
π^+	22	1.6
$\gamma(\pi^0)$	0	0
p	0	0
Sum	438	116

Table 7: Cherenkov trigger rates for ^{48}Ca target at 80 μA is estimated using simulated pion rejection and electron efficiency values from Fig. 28.

5.2.5 Data Acquisition

Due to the large number of channels and the necessity to keep the readout size small, the data acquisition system for SoLID is complex, even for the inclusive, independent-sector running for a PVDIS measurement. To approach this, SoLID utilizes pipelined electronics similar to the Hall D GlueX design. The readout for the calorimeter and Cherenkov is a VME JLAB FADC250 16-channel 12-bit FAC sampling at 250 MHz and a schematic of the FADC crate layout is shown in Fig. 30. VMM3 are currently being tested and will become the standard for GEM readout which is a pipelined readout system that will integrate with rest of the DAQ. A summary of channel and module counts per sector is shown Table 8.

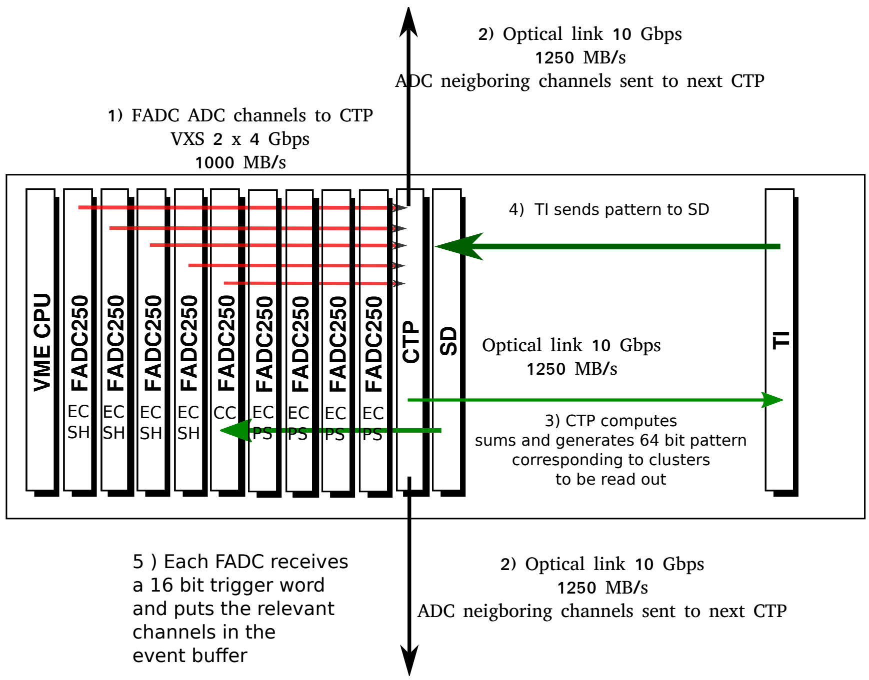

Figure 30: Layout of the FADC crate for the shower and preshower systems. Each crate contains a crate trigger processor (CTP), signal distribution module (SD), and trigger interface (TI).

Detector	Module Type	Number of Channels	Number of Modules
Electromagnetic Calorimeter (EC)	FADC	122	8
Light Gas Cherenkov (GC)	FADC	9	1
GEM	VME	4700	3

Table 8: Detector channel counts for each sector.

For our experiment, we anticipate about a total 155 kHz coincidence trigger, Table 9, for all sectors using both the calorimeter and gas Cherenkov signal compared to the 500 kHz trigger for the LD_2 measurement. We will run the 30 sectors independently requiring about 5 kHz/sector for the primary measurement.

A level 1 trigger can be formed by summing all modules for all sectors simultaneously every 4 ns and sending the signal to the crate trigger processor (CTP). To account for overlapping sectors on the calorimeter plane, neighboring CTPs are connected through optical links to share the overlapping 16 channels. Sup-

Particle	DAQ Coincidence Trigger Rate (kHz)	
	P > 1 GeV	P > 3 GeV
DIS e^-	144	61
π^-	11	7
π^+	0.4	0.2
Total	155	68

Table 9: Breakdown of coincidence trigger rates (Cherenkov+EM calorimeter) for momentuma > 1 GeV from ^{48}Ca target at $80\ \mu$A.

pression will be invoked on hits outside of a cluster. The gas Cherenkov configuration is similar but less complicated as each PMT array is unique to a sector and there is no overlap.

The VMM3 is currently being tested and will become the standard for GEM readout. This allows for a deadtime-less readout of the GEM signals. The DAQ system interfaces with the VMM3 chips to handle triggering of the readout, data transfer, and event building.

The data is then fed to the level 3 farm for data reduction. For this experiment the level 1 event data size is expected to be less than 50 kB with a 200 kHz level 1 rate. Further data reduction will be done correlating detectors such as the GEMs and calorimeter clusters together in space and time. Afterwards, crude track reconstruction must be performed for the GEMs. In particular, this is important for the GEM data rates as the occupancy will be on the order of 10-20%, or $\sim$3000 hits, making full hit recording untenable.

5.3 Polarimetry

A precise determination of the beam polarization is required to relate the asymmetry to the underlying physics measurement. As our statistical precision is about 1%, we require an uncertainty from the polarization better than that. We will utilize two independent techniques to measure this, Compton and Møller polarimetry. The upgrade to the existing Hall A Compton polarimeter is expected to provide a 0.4% precision. The MOLLER collaboration intends to improve precision of the existing Møller polarimeter to 0.4%.

5.4 Tracking, Optics, and Calibration

To precisely determine the kinematics of individual scattering events, tracking must first be performed using the GEM chambers and calorimeter, and then a sufficient optics model must be in place to reconstruct the event. In particular, the momentum p, scattering angle θ, and the scattering vertex along them beamline z must be known to sufficient precision to determine x and Q^2 as well as eliminate background window scattering events or events that originate outside of the target. Due to the relatively high luminosity and large acceptance for the experiment, efficient and fast tracking is important.

The overall background rates for this experiment are generally a factor of 2 smaller than the LD_2 experiment and therefore less demanding. As this is an inclusive measurement, tracking only needs to be done across a single sector. Presently, simulations are underway testing several tracking algorithms under the SoLID experimental conditions. These include a detailed model of SoLID and the individual GEM planes as well as a model detailing the ionization and GEM front-end electronics response based on real data [60] implementing an existing framework used for the Super Bigbite project, [61]. Those studies have shown 90% track reconstruction efficiency in occupancies that exceed the worst-case estimates of SoLID.

One additional challenge of the SoLID experiments is to reduce the data rate so at least crude tracking must be done “on the fly”. This requires extensive simulation and testing of reconstruction algorithms before the experiment can run. The SoLID collaboration is actively working at realizing this.

Optics models were implemented based on ray-traced tracks in the Geant4 simulation using a field map generated by the Poisson/Superfish package with a realistic coil and yoke geometry. The 0th order terms were based on the trajectories of particles in a uniform field and then deviations were fit using first order polynomials of generic track parameters. It was determined for SoLID in the PVDIS configuration that the momentum resolution is multiple scattering limited and about 1%, the angular resolution is GEM resolution limited and 0.5%, and the beamline vertex resolution of 7 mm. The derived quantities Q^2 and x were 1.5% and 1% respectively.

The calibration of the system requires several steps. First, GEM alignment must be done using "straight through" tracks with the magnetic field off and a combination of a set of thin carbon foils to ensure accurate interaction vertex reconstruction and a sieve to ensure angle reconstruction. Second, we utilize elastic scattering from a liquid hydrogen target and lower the beam energy to 4.4 GeV. The position of the elastic peak provides a point of calibration and the magnetic field can be scanned to provide additional points.

To aid with the determination of radiative effects, independent aluminum targets with $x/X_0 = 1\%$, 5%, and 10% will be included. These will aid in the verification of scattering rate distributions under different radiative conditions and the overall unfolding procedure, which will be limited by the determination of quantity of event bin-migration.

5.5 Radiation Dose in the Hall

Radiation dose is generated from the ^{48}Ca target by direct electron beam interactions as well as scattered electrons making secondary interactions in the hall. The iron core of the solenoidal magnet provides self shielding for high energy neutrons and will help to reduce the site boundary radiation budget. There are more extensive radiation and shielding studies for all SoLID experiments underway by the collaboration to minimize the radiation to the hall and to site boundary. Based on preliminary studies the neutron radiation on superconducting coils are expected be an order of magnitude lower then the radiation dose limit for the coils. For reference, we compare radiation budget from the 12% ^{48}Ca target to the approved LD_2 measurement. For normalization, we note that we are requesting 66 days at 80 μA compared to the approved measurement of 60 days at 50 μA on an LD_2 target. Accounting for the higher current and increased radiation length (12% ^{48}Ca target), the total exposure in the hall is larger due to the higher Z and increased radiation length (see Table 10).

Experiment	Hall (rem/h)	Ceiling (rem/h)
^{48}Ca at 80 uA	24.5	2.3
LD2 at 50 uA	10.2	1.2
Increase (%)	140	87

Table 10: Radiation dose in the hall and at the ceiling is estimated for ^{48}Ca and deuterium (LD2) targets. The dose increase for ^{48}Ca running is also shown at the bottom row.

5.5.1 Site Boundary Dose Comparison

During the design of PREX and CREX experiments, we have made progress in developing a more realistic Geant4 simulation to estimate the radiation dose. After the conclusion of PREX and CREX, we have compared our simulation estimations with site boundary dose measurements. These measurements have shown that Geant4 simulations have consistently overestimated the expected boundary dose as shown in the Table 11. Based on the Geant4 simulations we conducted, we have estimated that boundary dose during our proposal beam period to be about 2.5 mrem without dedicated sky-shine shielding implemented. The final site boundary dose will further reduce after SoLID shielding design is further optimized as we progress.

Experiment	Top of the Hall Neutron Dose (m^{-2})	Estimated Boundary DOSE (mrem)	Measured Boundary DOSE (mrem)
PREX-I	4.50E+12	4.2	1.3
PREX-II	5.80E+12	2.0	1.2
CREX	1.50E+13	1.8	1.0
LD-PVDIS 6 GeV	1.90E+12	0.7	n/a
LD-PVDIS 11 GeV	3.40E+12	1.3	n/a
^{48}Ca-PVDIS 11 GeV	6.00E+12	2.5	n/a

Table 11: Neutron dose at the top of the hall enclosure and site boundary dose were estimated using Geant4 simulations for previously ran PREX-I, PREX-II, CREX and LD-PVDIS 6 GeV experiments. The RADCON has also estimated site boundary dose for these experiments. The Geant4 simulations we used has consistently overestimated the RADCON site boundary dose estimation for these experiments.

6 Projections, Uncertainties, and Beam Time Request

6.1 Statistical Uncertainty

Our statistical uncertainty are calculated for 66 days at 80 μA on a 95% isotopically pure 2.4 g/cm^2 ^{48}Ca target. The projected statistical uncertainties on $A_{\rm PV}$ for our x and Q^2 bins is shown in Fig. 14. This translates to a sensitivity in a_1 shown in Fig. 12 assuming the standard model for C_{1i} and C_{2i}. The $Ya_3/2$ term in Eq. 6 is small for our kinematics only contributes to about 5% to the asymmetry and approximately proportional to the a_1 term due to the small contributions from sea quarks.

6.2 Systematics

The total systematic uncertainties are summarized in Table 12 and discussed in the following subsections.

Effect	Uncertainty [%]
Polarimetry	0.4
$R^{\gamma Z}/R^{\gamma}$	0.2
Pions (bin-to-bin)	0.1-0.5
Radiative Corrections (bin-to-bin)	0.5-0.1
Total for any given bin	∼0.5-0.7

Table 12: Summary of the systematic error contributions to our measurement.

6.2.1 Polarimetry

Two independent polarimeters will be deployed for this experiment. A continuous monitoring of the polarization will be done by the upgraded Compton polarimeter, which is anticipated to give 0.4% systematic uncertainty using both the photon and electron detectors. The iron-foil Møller polarimeter will provide an additional measurement periodically, as it is invasive, but with a projected uncertainty of about 0.8%. We assume a 0.4% shared systematic for our measurement.

6.2.2 Pion Contamination

Our anticipated pion contamination to the electron signal based on the combined rejection factors in the Cherenkov and the preshower and shower counters is expected to be no worse than 4% in a given bin, but still making it an important effect. The contamination is worst at the highest x due to the increased difficulty of separating high energy pions from electrons, but better for the higher Q^2 bins at a fixed x due to the relative number of fewer pions at large angle. To make a correction this requires good characterization of the pion contamination and the pion asymmetry.

Pion contamination level can be determined to good accuracy by using the gas Cherenkov and preshower/shower to cross-check one another. There is a large phase space in which to characterize, including momentum and position, but also drifts over time. A fraction of triggers without the gas Cherenkov will be dedicated to characterize this.

The pion asymmetry in the 6 GeV Hall A PVDIS experiment was measured to be a few times smaller than and the same sign as the LD_2 asymmetry [62]. For our estimations, we will conservatively assume that the π^- asymmetry is zero. For this scenario, to control the total pion systematic to less than 0.5%, the fractional contribution must be known to to a relative 8% and the π^- asymmetry must be known to 10 ppm.

For the asymmetry across all our bins, this would require at least an additional dedicated 10 kHz over all sectors of dedicated pion triggers over the course of the run, which is relatively small. This rate would also be sufficient to generate statistics to verify the contamination rates with a drift on the order of hours. We assign a systematic of 0.1-0.5% bin-to-bin, larger at larger x.

6.2.3 Charge-Symmetric Background

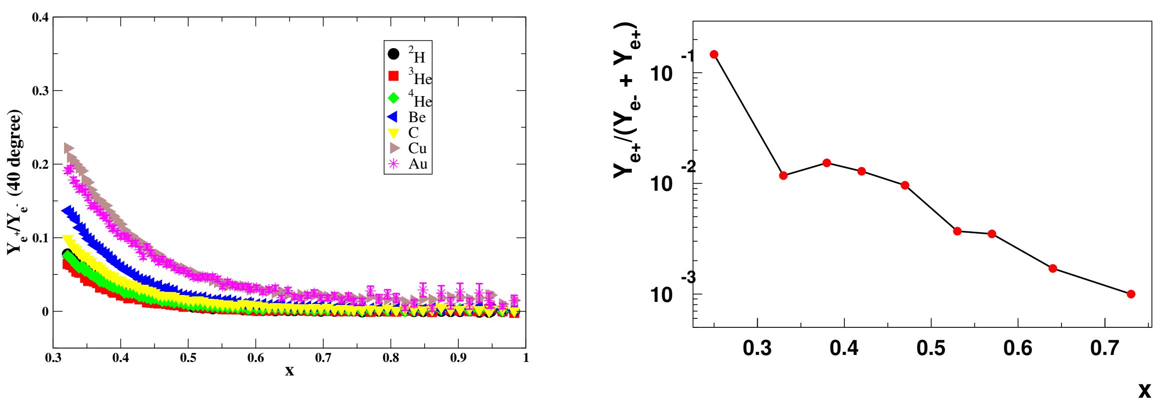

Figure 31: Charge-symmetric background at 5.77 GeV, 40 degrees, from E03-103 [18] (left). Expected charge-symmetric background for this experiment (evaluated at x and Q^2 values corresponding to Fig. 14), predicted using the model in Ref. [63] modified to agree with the Hall C E03-103 data (right).

Charge symmetric backgrounds in inclusive electron scattering are generated primarily from π^0 photo-production and the subsequent decay, $\pi^0 \rightarrow e^+e^-\gamma$. The electrons from this process can not be separated from those coming from DIS, so must be determined empirically via measurements of positron rates.

The charge symmetric background for this experiment was estimated using the model described in Ref. [63], tuned to agree with data taken as part of E03103 (see Fig. 31). The background is $\approx$15% at x=0.25, but decreases rapidly as x increases. This background is not expected to carry a significant asymmetry, but the dilution must be precisely determined to minimize the uncertainty on the final asymmetry. Dedicated measurements will be made with the solenoid polarity reversed to measure the charge symmetric background. At the lowest x, the positron yield should be measured to a relative precision of 1% to minimize impact on the final result. Four days have been have been requested to make measurements of the charge symmetric background: solenoid polarity changes (2 polarity changes, 1 day each including commissioning/checkout with beam), positive polarity production data (2 days).

Further checks of the model used to make the charge symmetric background estimates will be available after the upcoming run of E12-10-008 in Hall C, which will take data at kinematics similar to those in this proposal.

6.2.4 Radiative Corrections

Several factors need to be applied to extract the PDF-dependent quantities from our measured asymmetry. First, an unfolding procedure will need to be included to account for the hard radiative events. This causes the average Q^2 to be reduced, causes events from lower energy transfer (including resonant) events to become convoluted into the asymmetry. Fortunately, there is good momentum acceptance up to and even beyond elastic events, so these contributions will all be measured to sufficient accuracy within the Q^2 acceptance of the measurement. It was also shown that resonance event asymmetries are in general agreement with quark-hadron duality arguments [64].

The theory for radiative corrections is well understood e.g. [65], though for our kinematics calculations are ongoing by a dedicated working group within the collaboration. Up to 40% of the reconstructed DIS signal will come from resonance or migrated DIS and are worst for the lowest x bins. However, these events have asymmetries that are only a few percent different from the primary asymmetry which makes the corrections relatively small. We claim we can understand the size of the tails to at least 10% relative in the unfolding procedure, and we assign a 0.5%-0.1% bin-to-bin systematic, worse for small x.

The electroweak couplings, C_{iq}, are valid for all energy scales in the absence of radiative loop corrections. With these corrections, in one parameterization they become [26]

$$C_{1u} = \rho'_e \left(-\frac{1}{2} + \frac{4}{3}\hat{\kappa}'_e \hat{s}^2_Z\right) + \lambda' \tag{11}$$

$$C_{1d} = \rho'_e \left(\frac{1}{2} - \frac{2}{3}\hat{\kappa}'_e \hat{s}^2_Z\right) + 2\lambda' \tag{12}$$

$$C_{2u} = \rho_e \left(-\frac{1}{2} + 2\hat{\kappa}_e \hat{s}^2_Z\right) + \lambda_u \tag{13}$$

$$C_{2d} = \rho_e \left(\frac{1}{2} - 2\hat{\kappa}_e \hat{s}^2_Z\right) + \lambda_d \tag{14}$$

with, for $Q^2 \to 0$, $\rho'_e = 0.9887$, $\rho_e = 1.0007$, $\hat{\kappa}'_e = 1.0038$, $\hat{\kappa}_e = 1.0297$, $\lambda' = -1.8 \times 10^{-5}$, $\lambda_u = -0.0118$, $\lambda_d = 0.0029$, and $\hat{s}^2_Z = \sin^2\theta_W = 0.2312$. These are being calculated for our kinematics and are not likely to change in a way that is sensitive to this experiment.

6.2.5 Hadronic and Nuclear Uncertainties

There are potential contributions that can arise from higher order hadronic effects. Higher twist, charge symmetry violation (which mimics our isovector EMC effect in our signal), PDF uncertainties, and free PDF nuclear-model uncertainties can all potentially interfere with the extraction of a signal. Fortunately, these effects will be greatly constrained by approved measurements, within and outside of the SoLID program.

Charge symmetry violation will be measured in LD_2 to better precision than ours across the same kinematic range using the same apparatus, as described in Ref. [47] and are likely to be smaller than the proposed isovector EMC effect. If charge symmetry violation is found to be large in LD_2 or if the measurement here is found to be unexpectedly large, that may motivate a proposal similar to this one, but on ^{40}Ca. At present we assign no systematic uncertainty to charge symmetry violating effects.

$R = \sigma_L/\sigma_T$ has been determined for proton and deuterium DIS over a broad kinematic range, e.g. Ref. [66], and is about 0.2 for our kinematics. For our measurement of an asymmetry, the effects of this will mostly cancel, though one potential concern for this proposal is the nuclear dependence of of R. It has been suggested that these may be on the order of a few percent for our kinematics [67], which is negligibly small for our experiment due to cancellations and we ignore it.

For a symmetric target, specific higher twist effects can contribute in $A_{\rm PV}$ even though other Q^2 dependent effects such as the DGLAP evolution are highly suppressed. If they do turn out to be significant, the LD_2 measurement will provide constraints which then can be used as corrections to our measurement. For a 10% variation variation on a symmetric target at $Q^2 = 5$ GeV^2, these appear as a 0.5% correction to $A_{\rm PV}$ [68]. The LD_2 experiment uses a combination of 11 GeV and 6.6 GeV beam with the kinematic reach from 3 - 8 GeV^2 and as these effects to first order scale with $1/Q^2$, this provides a useful lever arm. We will be at high Q^2 kinematics and assign a shared systematic of 0.2% to our measurement.

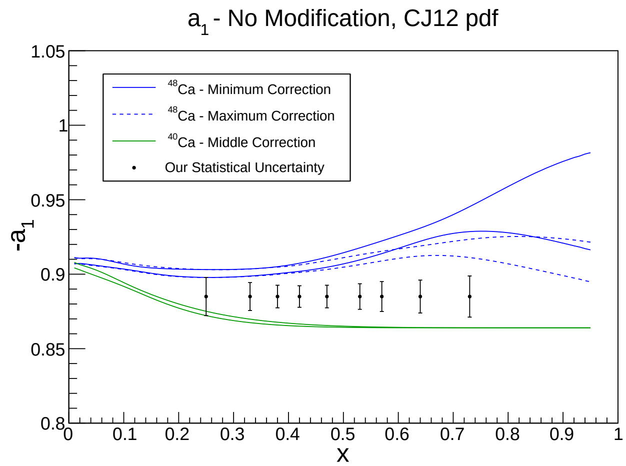

Figure 32: a_1 predictions from the CJ12 PDF fit [69] assuming no modification for ^{40}Ca, ^{48}Ca with different nuclear correction sizes.

6.2.6 Uncertainties from Free Parton Distributions

If the free parton distributions are not well constrained for our kinematics, either due to insufficient data or model-dependent nuclear corrections, it presents an effective systematic when testing for modification. While individual flavors are often shown to be well constrained by themselves, we are pursuing an unusual combination which requires careful consideration. We choose the recent CJ12 set [69] and make calculations for a_1 assuming that there is no modification, but appropriately weighting for Z and N. The results with our projected statistical uncertainties are shown in Fig. 32.

The fit uncertainty in a_1 assuming no modification is on the order of or less than $\sim$1% from $0.2 < x < 0.7$ and is presently smaller than our statistical uncertainties. Of even greater importance at $x > 0.5$ is the uncertainty in the model dependence on extracting quark flavor distributions from nuclear targets. At $x \sim 0.7$, this becomes large enough that it is close to the uncertainty on our largest error bar. Precision data from the SoLID proton program [47], BoNuS [70], and the ^{3}H/^{3}He ratio [52, 42] are sensitive to the ratio d/u, Fig. 33 and will constrain the uncertainties on a_1 for ^{48}Ca from the free PDFs to better than 0.2%. The leading order ratio d/u was extracted from preliminary MARATHON F_2^n/F_2^p results and is also shown in Fig. 33

While the presence of these would reduce the sensitivity to the discussed isovector EMC effect, ultimately, we are performing a measurement to be included into the global nuclear PDF fits. If this measurement is statistically incompatible with the models within those fits, then they must be revised. To this end, we assign no systematic uncertainty from this to our measurement, but make the comment that the uncertainties from the CJ12 fits when combined with upcoming d/u data will propagate to a_1 in ^{48}Ca in our x range to better than 0.2%.

6.2.7 Beam Parameters

Corrections to the measured asymmetry from helicity-correlated beam parameters are likely to be small due to the existing excellent beam quality at Jefferson Lab, the level of control at systematically reducing these errors, such as the double Wien filter, and the relative size of our asymmetry, which is on the order of 10^{-4} compared to the 10^{-6} level for experiments such as Qweak and PREX. Corrections are likely to be on the 0.1% level.

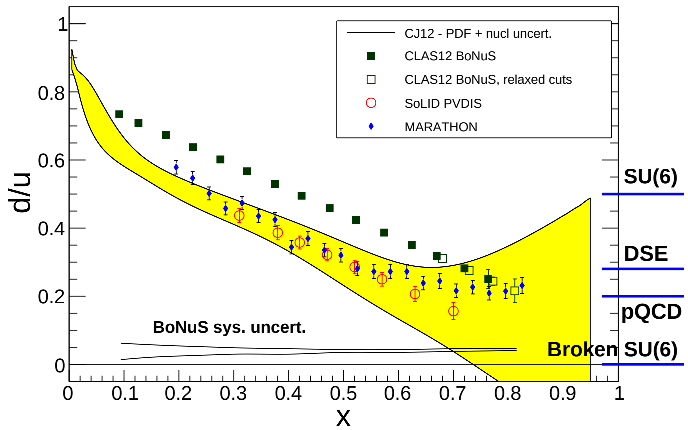

Figure 33: Anticipated data for measurements on d/u, see text for references. The constraints provided by these data will allow for accurate tests of an isovector EMC effect at larger x. The leading order ratio d/u was extracted from recently published MARATHON [42] F_2^n/F_2^p results are also shown

We have estimated an upper limit for beam normal spin asymmetry for ^{48}Ca using semi-empirical formula based on results from CREX experiment and found out to be -100 ppm. We are expecting less than 5% transverse leakage during production running. The azimuthal symmetry of the SoLID detectors will provide symmetry suppression factor of about 500. This was based on observed symmetry suppression during Qweak experiment. Based on transverse leakage and symmetry suppression factor we are expecting about -0.01 ppm residual beam normal spin asymmetry which is a negligible effect for a PVDIS asymmetry measurement.

6.3 Beam Time Request

We request 66 days of production data at 11 GeV at 80 μA with full beam polarization. We also request time for commissioning, calibration and background runs, and polarimetry, summarized in Table 13.

Table 13: Beam time request for this experiment.The positive polarity running includes 1 day per polarity change of the SoLID magnet.

	Time (days)	E (GeV)	Current (μA)
^{48}Ca Production	66	11	80
Optics	2	4.4	Up to 80
Positive polarity	4	11	80
Moller Polarimetry	4	11	2
Commissioning	5	11	Up to 80
Total	81		

A Quark Parton Model

In Eq. 6 higher order corrections for Y_1 and Y_3 were neglected and the Callan-Gross relation $F_2 = 2xF_1$ was invoked. Here we follow the convention of Ref. [68]. We define

$$R^{\gamma(\gamma Z)} \equiv \frac{\sigma_L^{\gamma(\gamma Z)}}{\sigma_T^{\gamma(\gamma Z)}} = r^2 \frac{F_2^{\gamma(\gamma Z)}}{F_1^{\gamma(\gamma Z)}} - 1 \tag{15}$$

$$r^2 = 1 + \frac{Q^2}{\nu} = 1 + \frac{4M^2x^2}{Q^2} \tag{16}$$

The full parity-violating asymmetry is in terms of the structure functions $F_1^{\gamma}(\gamma Z)$ and $F_2^{\gamma}(\gamma Z)$

$$A_{\rm PV} = -\left(\frac{G_F Q^2}{4\sqrt{2}\pi\alpha}\right) \frac{g_A^e \left(2xyF_1^{\gamma Z} - 2\left[1 - 1/y + xM/E\right] F_2^{\gamma Z}\right) + g_V^e x(2-y)F_3^{\gamma Z}}{2xyF_1^{\gamma} - 2\left[1 - 1/y + xM/E\right] F_2^{\gamma}} \tag{17}$$

We can then write it in the reduced from by

$$A_{\rm PV} = -\left(\frac{G_F Q^2}{4\sqrt{2}\pi\alpha}\right) \left[g_A^e Y_1 \frac{F_1^{\gamma Z}}{F_1^{\gamma}} + \frac{g_V^e}{2} Y_3 \frac{F_3^{\gamma Z}}{F_1^{\gamma}}\right] \tag{18}$$

with

$$Y_1 = \frac{1 + (1-y)^2 - y^2\left(1 - r^2/(1+R^{\gamma Z})\right) - 2xyM/E}{1 + (1-y)^2 - y^2\left(1 - r^2/(1+R^{\gamma})\right) - 2xyM/E} \left(\frac{1+R^{\gamma Z}}{1+R^{\gamma}}\right) \tag{19}$$

$$Y_3 = \frac{1 - (1-y)^2}{1 + (1-y)^2 - y^2\left(1 - r^2/(1+R^{\gamma})\right) - 2xyM/E} \left(\frac{r^2}{1+R^{\gamma}}\right) \tag{20}$$

and

$$F_1^{\gamma} = \frac{1}{2}\sum_i e_i^2 \left(q_i(x) + \bar{q}_i(x)\right); F_2^{\gamma} = 2xF_1^{\gamma}, \tag{21}$$

$$F_1^{\gamma Z} = \sum_i e_i g_V^i \left(q_i(x) + \bar{q}_i(x)\right); F_2^{\gamma Z} = 2xF_1^{\gamma Z}, \tag{22}$$

$$F_3^{\gamma Z} = 2\sum_i e_i g_A^i \left(q_i(x) - \bar{q}_i(x)\right). \tag{23}$$

References

[1] I. C. Cloet, W. Bentz, and A. W. Thomas. Isovector EMC effect explains the NuTeV anomaly. *Phys. Rev. Lett.*, 102:252301, 2009.

[2] Ian C. Cloet and Gerald A. Miller. Nucleon form factors and spin content in a quark-diquark model with a pion cloud. *Phys. Rev. C*, 86:015208, 2012.

[3] J. Arrington, A. Daniel, N. Fomin, and D. Gaskell. Detailed studies of the nuclear dependence of F2 in light nuclei. JLab experiment E12-10-008, 2010.

[4] I. C. Cloet, W. Bentz, and A. W. Thomas. Parity-violating DIS and the flavour dependence of the EMC effect. *Phys. Rev. Lett.*, 109:182301, 2012.

[5] John Arrington. Short-range correlations and their implications for isospin-dependent modification of nuclear quark distributions. *EPJ Web Conf.*, 113:01011, 2016.

[6] E. P. Segarra, A. Schmidt, T. Kutz, D. W. Higinbotham, E. Piasetzky, M. Strikman, L. B. Weinstein, and O. Hen. Neutron Valence Structure from Nuclear Deep Inelastic Scattering. *Phys. Rev. Lett.*, 124(9):092002, 2020.

[7] B. Schmookler et al. Modified structure of protons and neutrons in correlated pairs. *Nature*, 566(7744):354–358, 2019.

[8] J. Arrington and N. Fomin. Searching for flavor dependence in nuclear quark behavior. *Phys. Rev. Lett.*, 123(4):042501, 2019.

[9] E. P. Segarra, J. R. Pybus, F. Hauenstein, D. W. Higinbotham, G. A. Miller, E. Piasetzky, A. Schmidt, M. Strikman, L. B. Weinstein, and O. Hen. Short-Range Correlations and the Nuclear EMC Effect in Deuterium and Helium-3. *arXiv:2006.10249*, 2020.

[10] E. P. Segarra et al. The CLAS12 Backward Angle Neutron Detector (BAND). *Nucl. Instrum. Meth. A*, 978:164356, 2020.

[11] X. G. Wang, A. W. Thomas, and W. Melnitchouk. Do short-range correlations cause the nuclear EMC effect in the deuteron? *Phys. Rev. Lett.*, 125(26):262002, 2021.

[12] John Arrington, Aji Daniel, Donal Day, Nadia Fomin, Dave Gaskell, and Patricia Solvignon. A detailed study of the nuclear dependence of the EMC effect and short-range correlations. *Phys. Rev.*, C 86:065204, 2012.

[13] Donald F. Geesaman, K. Saito, and Anthony William Thomas. The nuclear EMC effect. *Ann. Rev. Nucl. Part. Sci.*, 45:337–390, 1995.

[14] P. R. Norton. The EMC effect. *Rept. Prog. Phys.*, 66:1253–1297, 2003.

[15] Simona Malace, David Gaskell, Douglas W. Higinbotham, and Ian Cloet. The Challenge of the EMC Effect: existing data and future directions. *Int. J. Mod. Phys. E*, 23(08):1430013, 2014.

[16] D. Dutta, J. C. Peng, I. C. Cloet, and D. Gaskell. Pion-induced Drell-Yan processes and the flavor-dependent EMC effect. *Phys. Rev. C*, 83:042201, 2011.

[17] J. Arrington, D. W. Higinbotham, G. Rosner, and M. Sargsian. Hard probes of short-range nucleon-nucleon correlations. *Prog. Part. Nucl. Phys.*, 67:898–938, 2012.

[18] J. Seely et al. New measurements of the EMC effect in very light nuclei. *Phys. Rev. Lett.*, 103:202301, 2009.

[19] N. Fomin et al. New measurements of high-momentum nucleons and short-range structures in nuclei. *Phys. Rev. Lett.*, 108:092502, 2012.

[20] L. B. Weinstein, E. Piasetzky, D. W. Higinbotham, J. Gomez, O. Hen, and R. Shneor. Short Range Correlations and the EMC Effect. *Phys. Rev. Lett.*, 106:052301, 2011.

[21] J. T. Londergan, J. C. Peng, and A. W. Thomas. Charge Symmetry at the Partonic Level. *Rev. Mod. Phys.*, 82:2009–2052, 2010.

[22] J. J. Aubert et al. The ratio of the nucleon structure functions $F2_n$ for iron and deuterium. *Phys. Lett. B*, 123:275–278, 1983.

[23] J. Gomez et al. Measurement of the A-dependence of deep inelastic electron scattering. *Phys. Rev. D*, 49:4348–4372, 1994.

[24] R. Subedi et al. Probing Cold Dense Nuclear Matter. *Science*, 320:1476–1478, 2008.

[25] Nadia Fomin, Douglas Higinbotham, Misak Sargsian, and Patricia Solvignon. New Results on Short-Range Correlations in Nuclei. *Ann. Rev. Nucl. Part. Sci.*, 67:129–159, 2017.

[26] J. Beringer et al. Review of Particle Physics (RPP). *Phys. Rev. D*, 86:010001, 2012. Section 10,Electroweak model and constraints on new physics.

[27] G. P. Zeller et al. A Precise Determination of Electroweak Parameters in Neutrino Nucleon Scattering. *Phys. Rev. Lett.*, 88:091802, 2002. [Erratum: Phys.Rev.Lett. 90, 239902 (2003)].

[28] E. A. Paschos and L. Wolfenstein. Tests for Neutral Currents in Neutrino Reactions. *Phys. Rev. D*, 7:91–95, 1973.

[29] `http://home.fnal.gov/~gzeller/nutev.html`.

[30] I. Schienbein, J. Y. Yu, C. Keppel, J. G. Morfín, F. Olness, and J. F. Owens. Nuclear parton distribution functions from neutrino deep inelastic scattering. *Phys. Rev. D*, 77:054013, 2008.

[31] I. Schienbein, J. Y. Yu, K. Kovarik, C. Keppel, J. G. Morfin, F. Olness, and J. F. Owens. PDF Nuclear Corrections for Charged and Neutral Current Processes. *Phys. Rev. D*, 80:094004, 2009.

[32] K. Kovarik, I. Schienbein, F. I. Olness, J. Y. Yu, C. Keppel, J. G. Morfin, J. F. Owens, and T. Stavreva. Nuclear Corrections in Neutrino-Nucleus DIS and Their Compatibility with Global NPDF Analyses. *Phys. Rev. Lett.*, 106:122301, 2011.

[33] Daniel de Florian, Rodolfo Sassot, Pia Zurita, and Marco Stratmann. Global Analysis of Nuclear Parton Distributions. *Phys. Rev. D*, 85:074028, 2012.

[34] Hannu Paukkunen and Carlos A. Salgado. Compatibility of neutrino DIS data and global analyses of parton distribution functions. *JHEP*, 07:032, 2010.

[35] Hannu Paukkunen and Carlos A. Salgado. Agreement of Neutrino Deep Inelastic Scattering Data with Global Fits of Parton Distributions. *Phys. Rev. Lett.*, 110(21):212301, 2013.

[36] B. Z. Kopeliovich, J. G. Morfin, and Ivan Schmidt. Nuclear Shadowing in Electro-Weak Interactions. *Prog. Part. Nucl. Phys.*, 68:314–372, 2013.

[37] D. Dutta, D. Gaskell, K. Hafidi, et al. Precise Measurement of pi+/pi- Ratios in Semi-inclusive Deep Inelastic Scattering Part II: Unraveling the Flavor Dependence of the EMC Effect. JLab Proposal PR12-09-004, 2009.

[38] D. Gaskell et al. LOI: Next Generation Tritium Experiments in CLAS12. JLab Letter of Intent LOI12-19-005, 2019.

[39] Jan Fredrich et al. COMPASS++/AMBER: Proposal for Measurements at the M2 beam line of the CERN SPS Phase-1: 2022-2024. *CERN-SPSC-2019-022 ; SPSC-P-360*, 2019.

[40] B. Adams et al. Letter of Intent: A New QCD facility at the M2 beam line of the CERN SPS (COMPASS++/AMBER). *arXiv:1808.00848*, 8 2018.

[41] Iraj Ruhi Afnan, Francois Rene Pierre Bissey, J. Gomez, A. T. Katramatou, Simonetta Liuti, W. Melnitchouk, G. G. Petratos, and Anthony William Thomas. Deep inelastic scattering from A = 3 nuclei and the neutron structure function. *Phys. Rev. C*, 68:035201, 2003.

[42] D. Abrams et al. Measurement of the Nucleon F_2^n/F_2^p Structure Function Ratio by the Jefferson Lab MARATHON Tritium/Helium-3 Deep Inelastic Scattering Experiment. *arXiv:2104.05850*, 2021.

[43] Sergey A. Kulagin and R. Petti. Global study of nuclear structure functions. *Nucl. Phys. A*, 765:126–187, 2006.

[44] S. A. Kulagin and R. Petti. Structure functions for light nuclei. *Phys. Rev. C*, 82:054614, 2010.

[45] E. P. Segarra et al. Nucleon off-shell structure and the free neutron valence structure from A=3 inclusive electron scattering measurements. *arXiv:2104.07130*, 2021.

[46] C. Cocuzza, C. E. Keppel, H. Liu, W. Melnitchouk, A. Metz, N. Sato, and A. W. Thomas. Isovector EMC effect from global QCD analysis with MARATHON data. *arXiv:2104.06946*, 2021.

[47] P. Souder et al. Precision Measurement of Parity-Violation in Deep Inelastic Scattering Over a Broad Kinematic Range. JLab experiment E12-10-007, 2010.

[48] Andreas Aste, Cyrill von Arx, and Dirk Trautmann. Coulomb distortion of relativistic electrons in the nuclear electrostatic field. *Eur. Phys. J. A*, 26:167–178, 2005.

[49] P. Gueye et al. Coulomb distortion measurements by comparing electron and positron quasielastic scattering off C-12 and Pb-208. *Phys. Rev. C*, 60:044308, 1999.

[50] I. Cloet. private communication.

[51] R. B. Wiringa, R. Schiavilla, Steven C. Pieper, and J. Carlson. Nucleon and nucleon-pair momentum distributions in $A \leq 12$ nuclei. *Phys. Rev. C*, 89(2):024305, 2014.

[52] G. Petratos, J. Arrington, M. Katramatou, D. Meekins, and R. Ransome. Measurement of the F2n/F2p, d/u Ratios and A=3 EMC Effect in Deep Inelastic Scattering off the Tritium and Helium Mirror Nuclei. JLab experiment E12-10-103, 2010.

[53] `http://hallaweb.jlab.org/12GeV/SoLID/download/doc/solid_precdr.pdf`.

[54] J. Pumplin, D. R. Stump, J. Huston, H. L. Lai, Pavel M. Nadolsky, and W. K. Tung. New generation of parton distributions with uncertainties from global QCD analysis. *JHEP*, 07:012, 2002.

[55] D. E. Wiser. Ph.D Thesis, University of Wisconsin-Madison, 1977.

[56] J. Arrington, D. Day, D. Higinbotham, and P. Solvignon. Three-nucleon short range correlations studies in inclusive scattering for $0.8 < Q^2 < 2.8(GeV/c)^2$. JLab experiment E08-014, 2008.

[57] S. Riordan et al. Parity-violating measurement of the weak charge distribution of 48Ca to 0.02 fm accuracy. JLab experiment E12-12-004, 2012.

[58] D. Meekins. private communication.

[59] C. W. de Jager et al. The Super-Bigbite Spectrometer for Jefferson Lab Hall A, 2010. https://userweb.jlab.org/~mahbub/HallA/SBS/SBS-CDR_New.pdf.

[60] G.M. Urciuli, M. Capogni, and E. Cisbani. Note on GEM digitiation modeling. http://www.iss.infn.it/cisbani/atmp/gemc/code/.

[61] G. Cates, K. deJager, J. LeRose, B. Wojtsekhowski, et al. Progress Report on the Super-Bigbite Project, 2011. http://hallaweb.jlab.org/12GeV/SuperBigBite/SBS_CDR/Response_TR2.pdf.

[62] P. E. Reimer, K. Paschke, and X. Zheng. Precision Measurement of the Parity-Violating Asymmetry in Deep Inelastic Scattering off Deuterium using Baseline 12 GeV Equipment in Hall C. JLab proposal PR12-07-102, 2007.

[63] P. Bosted. Pair-Symmetric and Pion Backgrounds for EG1b. http://www.jlab.org/Hall-B/notes/clas_notes04/2004-005.pdf.

[64] D. Wang et al. Measurements of Parity-Violating Asymmetries in Electron-Deuteron Scattering in the Nucleon Resonance Region. *Phys. Rev. Lett.*, 111(8):082501, 2013.

[65] Luke W. Mo and Yung-Su Tsai. Radiative Corrections to Elastic and Inelastic e p and mu p Scattering. *Rev. Mod. Phys.*, 41:205–235, 1969.

[66] L. W. Whitlow, E. M. Riordan, S. Dasu, Stephen Rock, and A. Bodek. Precise measurements of the proton and deuteron structure functions from a global analysis of the SLAC deep inelastic electron scattering cross-sections. *Phys. Lett. B*, 282:475–482, 1992.

[67] Vadim Guzey, Lingyan Zhu, Cynthia E. Keppel, M. Eric Christy, Dave Gaskell, Patricia Solvignon, and Alberto Accardi. Impact of nuclear dependence of $R = \sigma_L/\sigma_T$ on antishadowing in nuclear structure functions. *Phys. Rev. C*, 86:045201, 2012.

[68] T. Hobbs and W. Melnitchouk. Finite-Q^2 corrections to parity-violating DIS. *Phys. Rev. D*, 77:114023, 2008.

[69] J. F. Owens, A. Accardi, and W. Melnitchouk. Global parton distributions with nuclear and finite-Q^2 corrections. *Phys. Rev. D*, 87(9):094012, 2013.

[70] S. Bueltmann et al. The Structure of the Free Neutron at Large x-Bjorken. JLab experiment E12-06-113, 2006.